Live cell-lineage tracing and machine learning reveal patterns of organ regeneration

Oriol Viader-Llargués[#§], Valerio Lupperger[¶], Laura Pola-Morell[#§], Carsten Marr[¶*] and Hernán López-Schier[#§*]

Unit Sensory Biology & Organogenesis, Helmholtz Zentrum München, Neuherberg, Germany

§*Laboratory of Sensory Cell Biology, CRG, Barcelona, Spain*

¶ *Institute of Computational Biology, Helmholtz Zentrum München, Neuherberg, Germany*

corresponding author for computational analysis: carsten.marr@helmholtz-muenchen.de

for all requests: hernan.lopez-schier@helmholtz-muenchen.de

Keywords: Epithelium / Regeneration / Self-organization / Machine learning

ABSTRACT

Despite the intrinsically stochastic nature of damage, sensory organs recapitulate normal architecture during repair to maintain function. Here we present a quantitative approach that combines live cell-lineage tracing and multifactorial classification by machine learning to reveal how cell identity and localization are coordinated during organ regeneration. We use the superficial neuromasts in larval zebrafish, which contain three cell classes organized in radial symmetry and a single planar-polarity axis. Visualization of cell-fate transitions at high temporal resolution shows that neuromasts regenerate isotropically to recover geometric order, proportions and polarity with exceptional accuracy. We identify mediolateral position within the growing tissue as the best predictor of cell-fate acquisition. We propose a self-regulatory mechanism that guides the regenerative process to identical outcome with minimal extrinsic information. The integrated approach that we have developed is simple and broadly applicable, and should help define predictive signatures of cellular behavior during the construction of complex tissues.

INTRODUCTION

Understanding organogenesis, organ morphostasis and regeneration is crucial to many areas of biology and medicine, including controlled organ engineering for clinical applications (Lancaster, MA., et al., 2013; Boj, et al., 2015; Sato, T., Clevers, H., 2015; Willyard, C., 2015). External tissues sustain continuous injury and must recurrently repair to maintain physiological function during the life of the organism (Levin, M. 2009). Structural reproducibility depends on the re-establishment of cell identity, number, localization and polarization. Two aspects of organ regeneration are the current focus of intense attention. First, how multiple cells interact to recapitulate organ architecture. Second, what is the mechanism that controls the correct reproduction of cell number and localization. Here we use the neuromasts of the superficial lateral line in larval zebrafish to gain a global perspective on sensory-organ regeneration. The neuromasts are ideally suited for this purpose because they are small and external, facilitating physical access and three-dimensional high-resolution videomicroscopy of every cell during extended periods. We have combined live single-cell tracking, cell-lineage tracing, pharmacological and microsurgical manipulations, and multidimensional data analysis by machine learning to identify features that predict cell-fate decisions during neuromast repair. Our comprehensive approach is simple and model independent, which should facilitate its application to other organs or experimental systems that are accessible to videomicroscopy. It should help reveal the basic rules that underlie how complex structures emerge from the collective behavior of cells.

RESULTS

Complete neuromast ablation is irreversible in larval zebrafish

The neuromasts of the superficial lateral line in zebrafish are formed by a circular cuboidal epithelium of 60-70 cells (López-Schier and Hudspeth, 2006; Ghysen and Dambly-Chaudière, 2007; Norden, C., 2017). Mechanoreceptive hair cells occupy the center of the organ, whereas non-sensory sustentacular supporting cells are found around and between the hair cells (Figure 1A). A second class of supporting cell called mantle cells forms the outer rim of the organ. The invariant spatial distribution of these three cell classes generates a radial symmetry (Figure 1B) (Pinto-Teixeira et al., 2015). Neuromasts also have an axis of planar polarity defined by the orientation of the hair-cells' apical hair bundle (Figure 1C) (Ghysen and Dambly-Chaudière, 2007; Wibowo et al., 2011). In addition to this geometric organization, cell-class number and proportions are largely constant, with around 40 sustentacular, 8-10 mantle, and 14-16 hair cells. Non-sensory cells can proliferate, whereas the sensory hair cells are postmitotic (López-Schier and Hudspeth, 2006; Ma et al., 2008; Cruz et al., 2015; Pinto-Teixeira et al., 2015). Finally, a string of interneuromast cells connects each neuromast along the entire lateral-line system (Figure 1A) (Ghysen and Dambly-Chaudière, 2007). Previous studies have extensively characterized the regeneration of the mechanosensory hair cells (Williamset al., 2000; Harris et al., 2003; López-Schier and Hudspeth, 2006; Hernández et al., 2006; Ma et al., 2008; Behra et al. 2009; Faucherre et al., 2009; Wibowo et al., 2011; Namdaran et al., 2012; Steiner et al., 2014; Jiang et al., 2014).

However, the regeneration of non-sensory cells remains largely unexplored. To obtain quantitative data of whole sensory-organ regeneration we developed an experimental assay that combines controllable neuromast damage, long-term videomicroscopy at cellular resolution, and live cell-lineage tracing. We used combinations of transgenic lines expressing genetically encoded fluorescent proteins that allow the precise quantification and localization of each cell class in neuromasts, and which also serve as a direct and dynamic readout of tissue organization. This is important because it enables to visualize cell-fate transitions in living specimens within the growing tissue at high temporal resolution. Specifically, the *Tg[alpl:mCherry]* line expresses cytosolic mCherry in the mantle and interneuromast cells (Figure 1D). The *Et(krt4:EGFP)sqgw57A* (hereafter SqGw57A) expresses cytosolic GFP in sustentacular cells (Figure 1E). The *Tg[-8.0cldnb:LY-EGFP]* (Cldnb:lynGFP) express a plasma-membrane targeted EGFP in the entire neuromast epithelium and in interneuromast cells (Figure 1F), and the *Tg[Sox2-2a-sfGFP]* (Sox2:GFP) expresses cytosolic GFP in all the supporting cells and the interneuromast cells (Figure 1G). For hair cells, we use *Et(krt4:EGFP)sqet4*(SqEt4) that expresses cytosolic GFP (Figure 1H), or the *Tg(myo6b:actb1-EGFP)*(Myo6b:actin-GFP) that labels filamentous actin (Figure 1I). These transgenic lines have been previously published, but are reproduced here for clarity and self-containment of this work (López-Schier and Hudspeth, 2006; Kondrychyn et al., 2011; Kindt et al., 2012; Shin et al., 2014; Steiner et al., 2014; Pinto-Teixeira et al., 2015).

To induce tissue damage in a controllable and reproducible manner, we used a nanosecond ultraviolet laser beam that was delivered to individual cells through a high numerical-aperture objective, which was also used for imaging. The stereotypic localization of the neuromasts along the zebrafish larva varies only marginally between individuals and during larval growth (Figure 1J) (Ledent, V., 2002; López-Schier and Hudspeth, 2004). This permits the unambiguous identification of the manipulated neuromast throughout the experiment, and the comparison between corresponding organs in different animals. Using Sox2:GFP 5 day-old zebrafish larvæ that ubiquitously express a nucleus-targeted red-fluorescent protein (H2B-RFP) (Figure 1K-L), we certified that laser-targeted cells are rapidly eliminated from the neuromast epithelium with no detectable collateral damage (Figure1 M-P and Movie 1). Having established a well-controlled injury protocol, we decided to probe the limits of neuromast regeneration. We first used specimens co-expressing Alpl:mCherry and Cldnb:lynGFP, which reveal all neuromast cells in green and the mantle cells in red (Figure 2A). We began by ablating entire neuromasts and assessed regeneration for 7 days (Figure 2B-E). Specifically, we looked at the response of flanking interneuromast cells because it has been demonstrated that they can proliferate and generate additional neuromasts, particularly upon loss of ErbB2 signaling (López-Schier and Hudspeth, 2005; Grant et al, 2005; Sánchez, 2016). Four hours post-injury (4 hpi) a wound remains evident at the target area (Figure 2B). One day post-injury (1 dpi), the damaged area was occupied by a thread of

Alpl:mCherry(+) cells, which based on marker expression are likely interneuromast cells (Figure2C). None of the removed neuromasts regenerated after 7 days (n=22) (Figure 2D-E). We obtained an identical outcome using the independent pan-supporting cell marker Sox2:GFP (n=9) (Figure 2F-J). Finally, incubation of Alpl:mCherry specimens with Bromodeoxy-Uridine (BrdU) to reveal the DNA synthesis that occurs prior to mitosis showed that interneuromast cells do not proliferate after neuromast ablation (Figure 2K-N) (Gratzner, 1982). These data indicate that in contrast to what occurs in embryos (Sánchez, 2016), the complete elimination of a neuromast is irreversible in larval zebrafish.

Neuromasts have isotropic regenerative capacity

To further explore neuromast repair we decided to use milder injury regimes. We systematically produced controlled damage of well-defined scale and location in double transgenic specimens that combine the supporting cell marker Cldnb:lynGFP and the mantle-cell marker Alpl:mCherry (Figure 3A-O). We found that ablation of the posterior half of the neuromast was followed by closure of the wound within 24 hours (Figure3 A-C). At 3 dpi, target neuromasts regained normal cell-class spatial distribution (n=6) (Figure 3D). At 7 dpi, neuromasts recovered approximately 70% of the normal cell number (Figure3 E,Z). We found no difference in speed and extent of regeneration after concurrently ablating the posterior half of neuromasts and flanking interneuromast cells (n=5) (Figure3 F-J,Z). The ablation of the posterior or the dorsal half of the epithelium resulted in identical outcome,

157 suggesting that neuromasts are symmetric in their regenerative capacity (n=6)
158 (Figure3 K-O,Z). Next, we assessed mantle-cell regeneration using a double
159 transgenic line expressing Sox2:GFP and Alpl:mCherry, which reveal mantle cells
160 in red and sustentacular cells in green (Figure 3P-Y). The complete elimination of
161 mantle cells was followed by their re-emergence 3 dpi (Figure 3Q-S), and the
162 reconstitution of the outer rim of the neuromast 7 dpi (n=15) (Figure 3T,Z). The
163 simultaneous ablation of the mantle cells and the adjacent interneuromast cells led to
164 identical outcome (n=6) (Figure 3U-Z). The ablation of the interneuromast cells in
165 fish co-expressing Sox2:GFP and Alpl:mCherry on one side of a neuromast (n=12),
166 or between two adjacent organs (n=8) did not trigger the proliferation of the
167 remaining interneuromast cells over a period of 7 days (Figure 3 - figure supplement
168 1A-J). Because the complete ablation of mantle cells leaves intact the sustentacular-
169 cell population, and the hair cells are postmitotic, these results yield three important
170 and novel findings: 1) interneuromast cells are not essential for neuromast
171 regeneration in larval zebrafish, although they may contribute to mantle cell
172 regeneration; 2) neuromasts have isotropic regenerative capacity; 3) sustentacular
173 cells are tri-potent progenitors able to self-renew and to generate mantle and hair
174 cells.
175
176 **Neuromast architecture recovers after severe loss of tissue integrity**
177 To test the limits of neuromast regeneration we systematically ablated increasing
178 numbers of cells. Extreme injuries that eliminated all except 1 to 3 cells almost

179 always led to neuromast loss (not shown), whereas ablations that left between 4 and
180 10 cells, reducing the organ to a combination of 2-3 mantle and 2-7 sustentacular
181 cells, allowed regeneration (Figure 4A-E,K). We found that after losing over 95% of
182 their cellular content, neuromasts recover an average of 45 cells at 7 dpi (or
183 approximately 70% of the normal cell count), with exceptional cases reaching 60
184 cells (equivalent to over 90% of a normal organ) (n=15) (Figure 4K). Regenerating
185 neuromasts became radial-symmetric as early as 3 dpi (Figure 4D), and had normal
186 cell-class composition and proportions 7 dpi (Figure 4L-M). Next, we concurrently
187 ablated 95% of the neuromast and the flanking interneuromast cells (Figure 4F-G).
188 This intervention was followed by a similar regeneration process, but lead to smaller
189 organs (n=6) (Figure 4H-J,N-P). These observations reinforce our previous
190 suggestion that interneuromast cells have a non-essential, yet appreciable
191 contribution to regeneration. Timed quantification of cell-class number and
192 localization showed a reproducible pattern of tissue growth and morphogenesis.
193 During the first 24 hpi, the intact cells rebuilt a circular epithelium (Figure 4B).
194 From 1dpi to 3 dpi, cell number increases rapidly and proportion is restored (Figure
195 4C,K-M). After 3 dpi, cell number increases at a slower pace (Figure 4K-M).
196 Importantly, each cell class assumes an appropriate position despite a much reduced
197 cell number (Figure 4E,J,L-P).
198
199 Next, we examined if the orthogonal polarity axes of the epithelium are re-
200 established after the severest of injuries. To assess tissue apicobasal polarity we used

a combination of transgenic lines that allows the observation of the invariant basal position of the nucleus and the apical adherens junctions (Figure 4Q-R) (Ernst et al., 2012; Harding and Nechiporuk, 2012; Hava et al., 2009). We found correct positioning of these markers in the regenerated epithelium (n=4), including the typical apicobasal constriction of the hair cells (Figure 4S-T). To assess epithelial planar polarity, we looked at hair-bundle orientation using fluorescent phalloidin, which revealed that 7 dpi the regenerated neuromasts were plane-polarized in a manner indistinguishable from unperturbed organs, with half of the hair cells coherently oriented in opposition to the other half (n=10) (Figure 4U-W). To test if plane-polarizing cues derive from an isotropic forces exerted by the interneuromast cells that are always aligned to the axis of planar polarity of the neuromast epithelium, we ablated these cells flanking an identified neuromast, and concurrently killed the hair cells with the antibiotic neomycin (Figure 4X-Y). In the absence of interneuromast cells regenerating hair cells recovered normal coherent planar polarity (n=16), suggesting the existence of alternative sources of polarizing cues (Figure 4Z). Collectively, these findings reveal that as few as 4 supporting cells can initiate and sustain integral organ regeneration.

Sustentacular and mantle cells have different regenerative potential

Injury in the wild is intrinsically stochastic. Thus, we hypothesized that the regenerative response must vary according to damage severity and location, but progress in a predictable manner. To test this assumption and unveil the underlying

223 cellular mechanism, we systematically quantified the behavior of individual cells by
224 high-resolution videomicroscopy. We conducted 15 independent three-dimensional
225 time-lapse recordings of the regenerative process using a triple-transgenic line co-
226 expressing Cldnb:lynGFP, SqGw57A and Alpl:mCherry (Figure 5A-B), ranging
227 from 65 to 100 hours of continuous imaging (each time point 15 minutes apart).
228 Starting immediately after the ablation of all except 4-10 cells, we tracked every
229 intact original cell (called founder cell) and their progeny (cellular clones) (Figure
230 5A and Movie 2). We followed a total 106 founder cells (76 sustentacular cells and
231 30 mantle cells). We tracked individual cells manually in space and time, recording
232 divisions and identity until the end of the recording, resulting in 763 tracks and
233 104,863 spatiotemporal cell coordinates (Figure 5A-B). Each clone was represented
234 as a tree to visualize the contribution of each founder cell to the resulting clones
235 (Figure 5C). We found that the majority of the founder sustentacular cells underwent
236 3 divisions and that some divided up to 5 times (Figure 5D). 14 out of 30 founder
237 mantle cells did not divide at all, and the rest divided once or, rarely, twice. Founder
238 sustentacular cells required on average 19±6 hours (mean±s.d., n=76) to divide,
239 whereas the founder mantle cells that divided required on average 27±5 hours,
240 (mean±s.d., n=30) (Figure 5E). Clones from founder sustentacular and founder
241 mantle cells were markedly different: founder sustentacular cells produced all three
242 cell classes (sustentacular, mantle and hair cells), whereas founder mantle cells
243 produced clones containing only mantle cells (Figure 5F). We categorized all cell
244 divisions according to the fate of the two daughter cells at the time of the following

245 division, or at the end of the time-lapse recording (Figure 5G). This analysis
246 revealed that 97% of the sustentacular-cell divisions were symmetric: 78% produced
247 two sustentacular cells (SS), 16% produced a pair of hair cells (HH), and 3%
248 generated two mantle cells (MM). Only 3% of the divisions were asymmetric,
249 generating one sustentacular and one mantle cell (SM) (n=307). All mantle-cell
250 divisions were symmetric (MM) (n=20). These observations further support the
251 conclusion that sustentacular cells are tri-potent progenitors.
252
253 Previous studies have firmly established that hair-cell regeneration is strongly
254 anisotropic because hair-cell progenitors develop almost exclusively in the polar
255 areas of horizontal neuromasts, elongating the macula in the dorsoventral direction
256 (Wibowo et al., 2011; Romero-Carvajal et al., 2015). Although our static images
257 suggest that neuromasts have isotropic regenerative capacity, we nevertheless
258 wondered whether regeneration of non-sensory cells is directional. To this end, we
259 fractioned the epithelium of horizontal neuromasts in four quarters of equal
260 dimension (dorsal, ventral, anterior and posterior) (Figure 6A-B), which reflects the
261 known functional territorialization of the neuromast epithelium based on the
262 expression of transgenic markers and Notch signaling (Ma et al., 2008; Wibowo et
263 al., 2011). We first assessed the spatial distribution of cell divisions during the first
264 60 hours of regeneration and found no pattern that would suggest regeneration
265 anisotropy (Figure 6A). However, 60 hpi, most divisions (74%) took place in the
266 dorsal and ventral (polar) quarters (Figure 6B). This is expected because later

divisions mainly produce hair cells from polar progenitors (Figure 4L,M). Thus, the regenerating epithelium is initially homogeneous and becomes territorialized 60 hpi. We reasoned that epithelial territorialization could occur either by the migration of similar cells that are scattered throughout the tissue, or by position-adaptive differentiation of an initially equivalent population of cells. To test these possibilities, we generated a virtual Cartesian coordinate system at the center of the neuromast to fit all founder cells at the beginning of regeneration (4hpi). Next, we analyzed the localization of their progeny 60 hpi (Figure 6C-H). We found that 60% of the progeny of anterior-localized founder cells were located in the anterior side of the resulting epithelium, whereas 64% of the progeny of posterior-located founder cells were found in the posterior side (Figure 6C-E). We also found that 72% of cells derived from dorsal founder cells and 74% of cells from ventral founder cells were located on the same side of the virtual dorsal/ventral midline (Figure 6F-H). Therefore, most of the clones remain ipsilateral to the founder cell. These results indicate that neuromasts have isotropic regenerative capacity and their territorialization occurs by location-adaptive cellular differentiation.

The sustentacular-cell population is tri-potent and plastic

To answer the long-standing question of whether the sustentacular-cell population is homogeneous and approach the problem of what determines symmetric versus asymmetric modes of division, we characterized the composition of all 72 clones from founder sustentacular cells. We found four types of clones: containing only

289 sustentacular cells (S), sustentacular and mantle cells (SM), sustentacular and hair
290 cells (SH), and all three cell classes (SHM) (Figure 6I). Of note, founder mantle
291 cells produced clones containing only mantle cells (M) (Figures 5G and 6I). We
292 observed that 37/72 of the clones from founder sustentacular cells were SH, 21/72
293 were S, 12/72 were SM, and 2/72 were SHM (Figure 6I-K). The proportion of each
294 clone type suggests that either the sustentacular-cell population is heterogeneous, or
295 that it is homogeneous but plastic. In searching for potential sources of clone
296 heterogeneity, we noted that in some developmental contexts cell-cycle length or
297 proliferative potential can determine the fate of the daughter cells (Calegari, F. et al.,
298 2005; Rossi, AM. et al., 2017). Therefore, we quantified the kinetics of proliferation
299 of founder sustentacular cells and of their daughters and compared them to clone
300 composition. We found 3 clear waves of cell divisions, each spaced by 8-10 hours
301 (Figure 7A), respectively peaking at 20h, 28h and 38h (Figure 7B-C), suggesting
302 that cell-cycle length is strictly regulated. Cell-cycle length in the 1st generation
303 peaks around 10 hours (9.8±3.3h, median±interquartile range (iqr)) (Figure 7C), but
304 it begins to increase and to vary in the 2nd generation (11.5±7.3h, median±iqr), and
305 more so in the 3rd generation (18.8±20.3h, median±iqr). To identify transition
306 points in cycle lengths, we tested the goodness of fit of a two-segment regression
307 model with variable change points. We found that the length of cell cycles is
308 initially around 11±3 hours (mean±s.d.) and slowly increases up to 47 hpi.
309 Afterwards, cell-cycle length increases more rapidly and is more variable
310 (Figure7D). To test if cell number influences cell-cycle length we used a similar

two-segment regression model to define when cell-cycle length loosens, and discovered that the vast majority of the cell cycles (76%) span 7-13h below a threshold of 24 cells (Figure7E). Above this threshold, cell-cycles lengths show large variation. With these data, we plotted proliferation kinetics against clone type, and found no significant difference between clones (Figure 7F-G). Thus, the length of the cell cycle or the proliferative potential of founder sustentacular cells cannot explain clone composition.

Machine learning identifies predictive features for cell-fate acquisition

Multiple extrinsic factors that vary in space and time could determine cell-fate choices. Because manual analysis of such multidimensional data might be biased or neglect certain factors we implemented a quantitative and unbiased computational approach based on machine learning to identify variables (features) that correlate with clone composition. The first step of the workflow is the extraction of spatiotemporal coordinates and cell-lineage information from the manual tracks of the videomicroscopic data sets (n=15) (Figure 8A). For each cell-track coordinate, we extracted 32 quantifiable features (Table 1), which were used to train the machine-learning algorithm. In a pre-analysis, we compared the performance of 20 algorithms (support vector machines, decision trees and nearest neighbor classifiers) in terms of accuracy and area under the curve (AUC) and chose the ensemble bagged tree random forest algorithm (Breiman, 2001) as the best performing method (Figure 8 - figure supplement 1). To avoid overfitting, we trained the random forest

using 14 samples to predict clone composition in the remaining sample in a round robin fashion. We evaluated the quality of predictions using Matthews correlation coefficient (MCC) to compensate for imbalances of clone frequencies (Figure 6K).

Table 1. List of prediction features with description. We used 32 mainly spatial and neighborhood specific features for the classification. Features are explained in the description column.

Feature name	Description
Absolut time	Hours post induction (hpi)
Absolute distance to center	Euclidean distance to the neuromast center
Average distance to H cell	-
Average distance to M cell	-
Average distance to S cell	-
Cell generation	Number of divisions that the cell has undergone
Founder Cell Type	-
Minimum distance to H cell	-
Minimum distance to M cell	--
Minimum distance to S cell	-
Movement angle to last division	Angle between current cell location, neuromast center and location of last cell division (or start of the movie in case of founder cell division)
Movement direction compared to center	Radial distance between current cell location and location of last cell division (or start of the movie in case of founder cell division). If the current location is nearer to the center the value is (+) in case it is further away the value is (-)
Movement distance since last division	Euclidean distance between current cell location and last cell division (or start of the movie in case of founder cell division)
Normalized distance to center	Radial distance of current cell location divided by the radial distance of the current furthest cell (to approximate the neuromast size)
Number of founder cells	-
Number of H cells	-
Number of H cells in 10 µm radius	-
Number of H cells in 20 µm radius	-
Number of H cells in 30 µm radius	-
Number of M cells	-
Number of M cells in 10 µm radius	-
Number of M cells in 20 µm radius	-
Number of M cells in 30 µm radius	-
Number of S cells	-
Number of S cells in 10 µm radius	-
Number of S cells in 20 µm radius	-
Number of S cells in 30 µm radius	-
Number of total cells	-
Polar angle	Polar angle is the counterclockwise angle between the x-axis, the neuromast center and the current cell location
Time to last division	Time to last division (or start of the movie in case of founder cell division)
X coordinate	-
Y coordinate	-

Using machine learning, we were able to predict the occurrence of SH vs. SM clones from a founder sustentacular cell with high accuracy (42 out of 49 correctly predicted clones, MCC=0.63±0.09, mean±s.d., n=15 bootstrapped samples), while neither SH nor SM clones could be discriminated when compared to S clones (Figure 8B). Of the 32 features that we used, those that best discriminated SH vs SM clones were the sustentacular cells' distance to the center of the epithelium, and the distance to the mantle cells (Figure 8C and Figure 8- figure supplement2). Next, we focused on the decision-making process of individual sustentacular cells at the time of their division. We trained a random forest to discriminate between SS, HH and SM/MM divisions in a pairwise fashion. The HH and SM/MM divisions were highly predictable (63 out of 66 divisions correctly predicted, MCC=0.91±0.07, mean±s.d., n=15 bootstrapped samples), while the discrimination between SS and HH or SM/MM divisions was much less accurate (Figure 8D). Again, the most informative features were the distance to the neuromast center and the distance to the mantle cells (Figure 8E, Figure 8- figure supplement 3). SM/MM divisions occur consistently at the outer perimeter of the neuromast (Figure 8F), whereas HH divisions take place near the center. Self-renewing SS divisions occupy the area between HH and SM/MM divisions. Interestingly, SM/MM divisions were never seen in the anterior-most region of the organ, suggesting that progenitor sustentacular cells are routed into generating mantle cells specifically in the perimetral areas that lack mantle cells but not elsewhere. Therefore, regenerating

neuromasts appear to sense cell-class composition and route cellular differentiation in a spatially regulated manner to regain cell-class proportion and distribution.

DISCUSSION

One long-standing goal of biological research is to understand the regeneration of tissues that are exposed to persistent environmental abrasion. Here we address this problem by developing a quantitative approach based on videomicroscopic cell tracking, cell-lineage tracing, and machine learning to identify features that predict cell-fate choices during organ regeneration. Using the superficial neuromasts in zebrafish, we demonstrate that a remarkably small group of resident cells suffices to rebuild a functional organ following severe disruption of tissue integrity. Our findings reveal that the sustentacular-cell population is tri-potent, and suggest that integral organ recovery emerges from multicellular organization employing minimal extrinsic information. Below, we discuss the evidence that supports these conclusions.

By systematically analyzing cellular behavior, we reveal a hierarchical regenerative process that begins immediately after injury. First, surviving founder cells reconstitute an epithelium. Second, sustentacular cells become proliferative and restore organ size. Cellular intercalation is rare. Third, daughter cells differentiate in a position-appropriate manner to recreate cell-class proportions and organ geometric order. Fourth, the epithelium returns to a homeostatic state that is characterized by

low mitotic rate. The milder damage regimes that eliminated one half of the epithelium show that neuromasts are symmetric in their regenerative capacity, and that they preferentially regenerate the cells that have been eliminated. Importantly, these findings, which rely on the quantitative spatiotemporal analysis of regeneration data, could not have been predicted from previous studies using static and largely qualitative information (Williams and Holder, 2000; López-Schier and Hudspeth, 2005; Dufourcq et al., 2006; López-Schier and Hudspeth, 2006; Ma et al., 2008; Wibowo et al., 2011; Wada et al., 2013; Steiner et al., 2014; Romero-Carvajal et al., 2015; Cruz et al., 2015; Pinto-Teixeira et al., 2015). An important corollary of these results is that neuromasts do not contain specialized cells that contribute dominantly to repair. We propose that progenitor behavior is a facultative status that every sustentacular cell can acquire or abandon during regeneration. We did not observe regenerative overshoot of any cell class (Agarwala et al., 2015), suggesting the existence of a mechanism that senses the total number of cells and the cell-class balance during tissue repair (Simon et al., 2009). Together with previous work, our results support the possibility that such mechanism is based on the interplay between Fgf, Notch and Wnt signaling (Ma et al., 2008; Wibowo et al., 2011; Wada et al., 2013; Romero-Carvajal et al., 2015; Dalle Nogare and Chitnis, 2017). Our combination of machine learning and quantitative videomicroscopy shows clear differences between sustentacular and mantle cells, but does not indicate heterogeneity within the sustentacular-cell population. However, further application of this integrated approach and new transgenic markers may reveal uncharacterized

405 cells in the neuromast. This may be expected given recent work that showed the
406 existence of a new cell class in neuromasts of medaka fish (Seleit et al., 2017). It is
407 technically challenging to consistently maintain fewer than 4 cells *in toto* without
408 eliminating the entire neuromast. Thus, we cannot rule out the possibility that a
409 single founder cell may be able to regenerate a neuromast. We show that the
410 complete elimination of a neuromast is irreversible in larval zebrafish. However,
411 Sánchez and colleagues have previously reported that interneuromast cells can
412 generate new neuromasts (Sánchez, 2016). By assaying DNA synthesis prior to
413 mitosis, we show that interneuromast cells do not proliferate after neuromast
414 ablation. These differences may be explained by differences in ablation protocols
415 (electroablation versus laser-mediated cell killing), the age of the specimens
416 (embryos versus early larva) or the markers used to assess cellular elimination.
417
418 We find that interneuromast cells are not essential for neuromast regeneration
419 because severely damaged organs recover all cell classes in the appropriate
420 localization in the absence of interneuromast cells. However, we systematically
421 observed smaller organs when interneuromast cells where ablated. These
422 observations suggest that these peripheral cells may yet help regeneration, either
423 directly by contributing progeny, or by producing mitogenic signals to neuromast-
424 resident cells. The behavior of the mantle cells is especially intriguing. Complete
425 elimination of parts of the lateral line by tail-fin amputation have revealed that
426 mantle cells are able to proliferate and generate a new primordium that migrates into

427 the regenerated fin to produce new neuromasts (Dufourcq et al., 2006). This
428 observation can be interpreted as suggesting that under some injury conditions,
429 mantle cells are capable of producing all the cell classes of a neuromast.
430 Transcriptomic profiling of mantle cells following neuromast injury revealed that
431 these cells up-regulate the expression of multiple genes (Steiner et al., 2014).
432 Furthermore, a recent study has revealed that mantle cells constitute a quiescent pool
433 of cells that re-enters cell cycle only in response to severe depletion of sustentacular
434 cells (Romero-Carvajal et al., 2015), suggesting that these cells may conform a
435 stem-cell niche for proliferation of sustentacular cells. Thus, the collective evidence
436 indicates that the mantle cells respond to damage and contribute to the regenerative
437 processes, and may drive the regeneration of an entire organ if every other cell class
438 is lost.
439
440 One outstanding question is how regeneration is controlled spatially. The epithelium
441 may respond to damage via dynamic formation of an injured-intact axis at the onset
442 of repair. Our results support this scenario by unveiling the adaptability of the
443 neuromast epithelium to the localization and scale of damage. We suggest a model
444 in which the invariant radial symmetry of the neuromast serves as a rheostat to
445 identify the site of damage to guide regeneration spatially (Figure 9). A polarized
446 axis along structurally intact and injured areas underlies this process. However, the
447 complete reconstruction of a neuromast by as few as 4 cells suggests that a partial
448 maintenance of radial symmetry is not essential for organ regeneration. Therefore,

449 radial-symmetry maintenance cannot have a deterministic impact on the recovery of
450 geometric order. Yet, partial structural maintenance and polarized tissue responses
451 may optimize repair, respectively, by preventing superfluous cellular production in
452 undamaged areas and by biasing the production of lost cells in the damaged areas.
453 For organs that have evolved under the pressure of persistent damage, compliance to
454 the extent of the injury may be an advantage because the regenerative responses can
455 be scalable and localized, allowing faster and more economical regeneration.
456
457 After the severest of injuries, regenerated neuromasts were plane polarized in a
458 manner indistinguishable from unperturbed organs. This startling result indicates
459 that as few as 4 founder supporting cells can re-organize the local coherent planar
460 polarity of the epithelium during neuromast repair. An alternative explanation is that
461 founder cells have access to external polarizing cues. One source of this information
462 is an isotropic mechanical forces exerted by the interneuromast cells that flank a
463 neuromast. This is possible because interneuromast cells are always aligned to the
464 neuromast's axis of planar polarity. Yet, the concurrent ablation of resident hair cells
465 and the interneuromast cells around an identified neuromast led to regenerated hair
466 cells whose local orientation was coherent. Interestingly, recent studies have
467 identified a transcription factor called Emx2 that regulates the orientation of hair
468 cells in neuromasts of the zebrafish (Jiang et al., 2017). Emx2 is expressed in one
469 half of the hair cells of the neuromast (those oriented towards the tail) and absent in
470 the other half (which are coherently oriented towards the head). Loss- and gain-of-

function of Emx2 alter planar cell polarity in a predictable manner: loss of Emx2 leads to neuromasts with every hair cells pointing towards the head of the animal, and Emx2 broad expression orients hair cells towards its tail. Because the coherent local axis of polarity is not affected by these genetic perturbations, Emx2 may act in hair cells as a decoder of global polarity cues. This evidence, together with our results, suggests that during neuromast regeneration founder cells autonomously organize the variegated expression of Emx2 in the regrowing epithelium with consequent recovery of a coherent axis of planar polarity and with one half of the hair cells pointing opposite to the other half. The future development of live markers of Emx2 expression will be able to test this prediction. We would like to highlight that we do not currently understand the global polarization of the neuromast epithelium relative to the main body axes of the animal. External sources of polarity may impinge in the recovery of these global axes during neuromast regeneration. Previous work has demonstrated that local and global polarization occur independently of innervation (López-Schier and Hudspeth, 2006), but other potential polarizing cues remain untested. Therefore, at present we can only support the notion that local coherent polarity is self-organizing, whereas global orientation may be controlled externally.

Our results beg the question of whether neuromast cells self-organize. Our operational definition of self-organization is an “autonomous increase in order by the sole interaction of the elements of the system” (Haken, 1983), implying that a

493 cellular collective organizes a complex structure without the influence of external
494 morphogenetic landmarks, patterning cues, or pre-existent differential gene-
495 expression profiles. If these conditions are not met, cellular groups may nevertheless
496 form a complex structure through a process of "self-assembly" (Sasai, 2013; Turner
497 et al., 2016). The reduction of neuromasts to around 5% of their original size shows
498 that intact resident cells can rapidly recreate their original microenvironment to
499 rebuild a neuromast with normal organization, proportions and polarity. Although
500 these observations suggest autonomy, extrinsic sources of information including the
501 extracellular matrix that remains intact after cell loss may serve as a blueprint for
502 epithelial organization. Yet, unless such patterns are rebuilt together with the organ,
503 neuromasts architecture and proportions would depend on the area occupied by the
504 regrowing epithelium. In other words, cell-fate acquisition and cell-class distribution
505 must be tissue-size dependent. However, we show that neuromast regain geometric
506 order as early as 2 days after injury, when their cellular content is less than 60% of
507 the original. Although our results do not irrefutably demonstrate self-organization
508 during neuromast regeneration, they strongly support this idea. We argue that self-
509 organization is an optimal morphogenetic process to govern organ repair because (i)
510 it requires the least amount of previous information and (ii) it is robust to run-off
511 signals that could lead to catastrophic failure.
512
513 **CONCLUSIONS**

Understanding how tissues respond to the inherently random nature of injury to recapitulate their architecture requires the identification of cues and signals that determine cell-fate acquisition, localization and three-dimensional organization. Here we reveal an archetypal sensory organ endowed with isotropic regenerative ability and responses that comply to damage severity, nature and location. An important corollary of our findings is that progenitor behavior is a facultative status that every progenitor cell can acquire or abandon during regeneration (Blanpain, C., Fuchs, E., 2014; Wymeersch, F.J., et al., 2016). Importantly, we illustrate a machine learning implementation to identify features that predict cell-fate choices during tissue growth and morphogenesis. This quantitative approach is simple and model-independent, which facilitates its application to other organs or experimental systems to understand how multiple cells interact dynamically during organogenesis and organ regeneration in the natural context of the whole animal, and to identify how divergences from the normal regenerative processes lead to failed tissue repair.

MATERIALS AND METHODS

Zebrafish strains and husbandry

Zebrafish were maintained under standard conditions, and experiments were performed in accordance with protocols approved by the PRBB Ethical Committee of Animal Experimentation of the PRBB Barcelona, Spain. Eggs were collected from natural spawning and maintained at 28.5°C in Petri dishes at a density of up to

50 per dish. Transgenic lines used were *ET(krt4:EGFP)SqGw57A* (referred to in the text as SqGw57A) (Kondrychyn et al., 2011), *ET(krt4:EGFP)SqET4* (SqET4) (Parinov et al., 2004), *Tg[Myo6b:actb1-EGFP]* (Kindt et al., 2012), *Tg[-8.0cldnb:Lyn-EGFP]* (Cldnb:lynGFP) (Haas and Gilmour, 2006), *Tg[Alpl:mCherry]* (Steiner et al., 2014), *Tg[Sox2-2a-sfGFPstl84]* (referred to as Sox2:GFP) (Shin et al., 2014). To label cell nuclei, *in vitro* transcribed capped RNA coding for histone 2B-mCherry was injected in 1-4 cell embryos at a concentration of 100ng/µl (Rosen et al., 2009). Throughout the study, zebrafish larvæ were anesthetized with a 610µM solution of the anesthetic 3-aminobenzoic acid ethyl ester (MS-222).

Laser-mediated cell ablations

For *in toto* cell ablation, we used the iLasPulse laser system (Roper Scientific SAS) mounted on a Zeiss Axio Observer inverted microscope equipped with a 63X water-immersion objective (N.A. = 1.2) (Xiao et al., 2015). The same ablation protocol was used for all experiments using 5 dpf larvæ. Briefly, zebrafish larvæ were anesthetized, mounted on a glass-bottom dish and embedded in 1% low-melting point agarose. Three laser pulses (355nm, 400 ps/2.5 µJ per pulse) were applied to each target cell. After beam delivery, larvæ were removed from the agarose and placed in anesthesia-free embryo medium. All ablations were systematically performed on the L2 or L3 posterior lateral-line neuromasts, except for those in Figure 6F, for which we targeted the LII.2 neuromast.

Phalloidin staining

557 Samples were fixed in 4% PFA overnight at 4°C, washed several times in 0.1%
558 PBSTw and incubated in phalloidin-Alexa 568 or Alexa 488 (Invitrogen) diluted
559 1:20 in 0.1% PBSTw overnight at 4°C. Samples were washed several times in 0.1%
560 PBSTw and mounted in 0.1% PBSTw with Vectashield (1/100, Vector Labs,
561 Burlingame, CA, USA).

562 **Regeneration analysis and quantification**

563 For quantification of cell numbers during neuromast regeneration,
564 *Tg[Cldnb:lynGFP; SqGw57A; Alpl:mCherry]* zebrafish larvæ were anesthetized,
565 mounted on a glass-bottom dish and embedded in 1% low-melting point agarose. All
566 samples were imaged before injury, 4 hpi and every 24 hours up to 7 dpi with an
567 inverted spinning-disc confocal microscope (Zeiss by Visitron), under a 63X water-
568 immersion objective. After imaging, larvæ were quickly transferred to anesthetic-
569 free medium. Cells were manually counted using the FIJI multi-point tool by
570 scrolling throughout the entire volume of the neuromast. Cell classes were identified
571 by the following criteria: Interneuromast cells: Cldnb:lynGFP(+), SqGw57A(-),
572 Alpl:mCherry(+). Mantle cells: Cldnb:lynGFP(+), SqGw57A(+), Alpl:mCherry(+).
573 Sustentacular cells: Cldnb:lynGFP(+), SqGw57A(+), Alpl:mCherry(-). Hair cells:
574 Cldnb:lynGFP(+), SqGw57A(-), Alpl:mCherry(-). Hair cell identity was verified by
575 the concomitant observation of the correct transgene expression pattern, central-
576 apical location and the presence of a hair-cell bundle. Data was processed and
577 analyzed using GraphPad Prism version 6.04 for Windows (GraphPad Software, La
578 Jolla, CA, USA, www.graphpad.com). In the box plots, the boundary of the box

579 closest to zero indicates the 25th percentile (q1), a black line within the box marks
580 the median, and the boundary of the box farthest from zero indicates the 75th
581 percentile (q3). Whiskers above and below the box include points that are not
582 outliers. Points are considered as outliers if they are bigger than q3 + 1.5(q3 – q1) or
583 smaller than q1 – 1.5(q3 – q1).

584 **Videomicroscopy, cell tracking and lineage tracing**

585 Larvæ were anesthetized, mounted onto a glass-bottom 3-cm Petri dish (MatTek)
586 and covered with 1% low-melting point agarose with diluted anesthetic. Z-stack
587 series were acquired every 15 minutes at 28.5°C using a 63X water-immersion
588 objective. Cells were tracked overtime using volumetric Z-stack images with FIJI
589 plugin MTrackJ (Meijering et al., 2012). Movies were registered two times for
590 image stabilization and centered upon the centroid of the surviving group of cells
591 and the subsequent regenerating organs. Founder cells are identified from 1 to 6 (*n*)
592 and their daughter cells receive *2n* and *2n+1* identities. All images were processed
593 with the FIJI software package.

594 **Pharmacology**

595 All pharmacological treatments were performed as described previously (López-
596 Schier and Hudspeth, 2006; Wibowo, 2011; Pinto-Teixeira et al., 2015). Briefly, the
597 following concentrations and timings used were: Neomycin sulfate (Sigma, St.
598 Louis, MO) 250µM for 45min; N-[N-(3,5-difluorophenacetyl)-L-alanyl]-S-
599 phenylglycine-t-butyl ester (DAPT) (Sigma) 100µM for 24-48h. Equal amounts of
600 DMSO were diluted in embryo medium for control specimens.

Random forest prediction

Random forest algorithms use the majority vote of numerous decision trees based on selected features to predict choices between given outcomes (Murphy, K. P., 2012.). We used a list of spatial, movement and neighborhood features (see Suppl. Table 1) to perform the random forest prediction of fate choice. We trained the random forest on 14 experiments and tested our prediction on one left-out experiment in a round robin fashion, leading to 15 test sets overall. To evaluate our prediction, we calculated Matthews correlation coefficient (MCC) (Matthews, 1975), which accounts for imbalance in our data (e.g. 78% of all divisions are SS divisions). The MCC is calculated by:

$$\mathrm{MCC} = \frac{TP \times TN - FP \times FN}{\sqrt{(TP + FP)(TP + FN)(TN + FP)(TN + FN)}}$$

where TP denotes true positive, TN true negative, FP true positive and FN false negative predictions. The MCC can have values between -1 and +1, where -1 is a completely incorrect, 0 a random and +1 a perfect prediction. To evaluate the variance of the MCC on the 15 test sets we used a bootstrapping approach, where we draw 15 samples from all test sets with replacement 15 times. From this resampled data we calculated the mean MCC and the standard deviation as shown in Figs. 8B and 8D. All machine-learning analyses were performed using MATLAB (Version 2015b on a Windows 7 machine)

ACKNOWLEDGEMENTS

We thank A. Steiner, T. Nicolson and L. Solnica-Krezel for transgenic zebrafish, the animal facility personnel at the CRG of Barcelona and the HMGU for animal care, and Kirill Smirnov for statistical support. Funding was provided by the European Research Council Grant 2007_205095, by the ESF Research Networking Programme "QuanTissue", and by the AGAUR Grant 2009-SGR-305 of Spain.

REFERENCES

Agarwala, S., Duquesne, S., Liu, K., Boehm, A., Grimm, Link, S., König, S., Eimer, S., Ronneberger, and Lecaudey, V. (2015). Amotl2a interacts with the Hippo effector Yap1 and the Wnt/β-catenin effector Lef1 to control tissue size in zebrafish. eLife *4*, e08201.

Behra M, Bradsher J, Sougrat R, Gallardo V, Allende ML, Burgess SM. (2009). Phoenix is required for mechanosensory hair cell regeneration in the zebrafish lateral line. PLoS Genet. *5*, e1000455.

Blanpain, C., and Fuchs, E. (2014). Stem cell plasticity. Plasticity of epithelial stem cells in tissue regeneration. Science *344*, 1242281.

Boj, S.F., Hwang, C.-I., Baker, L.A., Chio, I.I.C., Engle, Corbo, V., Jager, M., Ponz-Sarvise, M., Tiriac, H., Spector, M.S., et al. (2015). Organoid models of human and mouse ductal pancreatic cancer. Cell *160*, 324–338.

Breiman, L. (2001). Random Forests. Machine Learning *45*, 5–32.

643 Calegari, F., Haubensak, W., Haffner, C., Huttner ,W.B. (2005). Selective
644 lengthening of the cell cycle in the neurogenic subpopulation of neural progenitor
645 cells during mouse brain development. J. Neurosci. *25(28)*, 6533-6538.
646 Cruz, I.A., Kappedal, R., Mackenzie, S.M., Hailey, D.W., Hoffman, T.L., Schilling,
647 T.F., and Raible, D.W. (2015). Robust regeneration of adult zebrafish lateral line
648 hair cells reflects continued precursor pool maintenance. Dev. Biol. *402*, 229–
649 238.
650 Dalle Nogare D, Chitnis AB. (2017). A framework for understanding
651 morphogenesis and migration of the zebrafish posterior lat line primordium.
652 Mech. Dev. *148*, 69
653 Dufourcq, P., Roussigné, M., Blader, P., Rosa, F., Peyrieras, N., and Vriz, S. (2006).
654 Mechano-sensory organ regeneration in adults: the zebrafish lateral line as a
655 model. Mol. Cell. Neurosci. *33*, 180–187.
656 Ernst, S., Liu, K., Agarwala, S., Moratscheck, N., Avci, M.E., Dalle Nogare, D.,
657 Chitnis, A.B., Ronneberger, O., and Lecaudey, V. (2012). Shroom3 is required
658 downstream of FGF signalling to mediate proneuromast assembly in zebrafish.
659 Development *139*, 4571–4581.
660 Faucherre A, Pujol-Martí J, Kawakami K, López-Schier H. (2009). Afferent neurons
661 of the zebrafish lateral line are strict selectors of hair-cell orientation. PLoS ONE
662 *4*, e4477.
663 Ghysen, A., and Dambly-Chaudière, C. (2007). The lateral line microcosmos.
664 Genes Dev. *21*, 2118–2130.

665 Grant, K. A., Raible, D. W., & Piotrowski, T. (2005). Regulation of latent sensory
666 hair cell precursors by glia in the zebrafish lateral line. Neuron, 45(1), 69-80.
667 Gratzner, H.G. (1982). Monoclonal antibody to 5-bromo- and 5-iododeoxyuridine:
668 A new reagent for detection of DNA replication. Science *218*, 474-475.
669 Haas, P., Gilmour, D. (2006). Chemokine signaling mediates self-organizing tissue
670 migration in the zebrafish lateral line. Dev. Cell *10*, 673–680.
671 Haken H. (1983). Synergetics : Non-Equilibrium Phase Transitions and Self-
672 organization in Physics, Chemistry and Biology (3rd ed.), (Springer, Berlin).
673 Harding, M.J., and Nechiporuk, A.V. (2012). Fgfr-Ras-MAPK signaling is required
674 for apical constriction via apical positioning of Rho-associated kinase during
675 mechanosensory organ formation. Development *139*, 3130–3135.
676 Harris JA, Cheng AG, Cunningham LL, MacDonald G, Raible DW, Rubel EW.
677 (2003). Neomycin-induced hair cell death and rapid regeneration in the lateral
678 line of zebrafish (*Danio rerio*). J. Assoc. Res. Otolaryngol. *4(2)*, 219-234.
679 Hava, D., Forster, U., Matsuda, M., Cui, S., Link, B.A., Eichhorst, J., Wiesner, B.,
680 Chitnis, A., and Abdelilah-Seyfried, S. (2009). Apical membrane maturation and
681 cellular rosette formation during morphogenesis of the zebrafish lateral line. J.
682 Cell. Sci. *122*, 687–695.
683 Hernández PP, Moreno V, Olivari FA, Allende ML. (2006). Sub-lethal
684 concentrations of waterborne copper are toxic to lateral line neuromasts in
685 zebrafish (*Danio rerio*). Hear. Res. *213*, 1-10.

686 Jiang T, Kindt K, Wu DK. (2017). Transcription factor Emx2 controls stereociliary
687 bundle orientation of sensory hair cells. eLife. *7*, 6.
688 Kindt, K.S., Finch, G., and Nicolson, T. (2012). Kinocilia mediate
689 mechanosensitivity in developing zebrafish hair cells. Dev. Cell *23*, 329–341.
690 Kondrychyn, I., Teh, C., Garcia-Lecea, M., Guan, Y., Kang, A. and Korzh, V.
691 (2011). Zebrafish Enhancer TRAP transgenic line database ZETRAP 2.0.
692 Zebrafish *8*, 181.
693 Lancaster, M.A., Renner, M., Martin, C.-A., Wenzel, D., Bicknell, L.S., Hurles,
694 M.E., Penninger, J.M., Jackson, A.P., and Knoblich, J.A. (2013). Cerebral
695 organoids model human brain development and microcephaly. Nature *501*, 373.
696 Ledent, V. (2002). Postembryonic development of the posterior lateral line in
697 zebrafish. Development *129,* 597–604
698 Levin, M. (2009). Errors of Geometry: Regeneration in a broader perspective.
699 Seminars in Cell & Developmental Biology *20*, 643–645.
700 López-Schier, H., Starr, C.J., Kappler, J.A., Kollmar, R., Hudspeth, A.J. (2004).
701 Directional cell migration establishes the axes of planar polarity in the posterior
702 lateral-line organ of the zebrafish. Dev. Cell. 7(3):401-12.
703 López-Schier, H., and Hudspeth, A.J. (2005). Supernumerary neuromasts in the
704 posterior lateral line of zebrafish lacking peripheral glia. Proc. Natl. Acad. Sci.
705 U.S.A. *102*, 1496–1501.

López-Schier, H., and Hudspeth, A.J. (2006). A two-step mechanism underlies the planar polarization of regenerating sensory hair cells. Proc. Natl. Acad. Sci. U.S.A. *103*, 18615–18620.

Ma, E.Y., Rubel, E.W., and Raible, D.W. (2008). Notch signaling regulates the extent of hair cell regeneration in the zebrafish lateral line. J. Neurosci. *28*, 2261.

Matthews, B.W. (1975). Comparison of the predicted and observed secondary structure of T4 phage lysozyme. Biochim Biophys Acta, 405(2), 442-451.

Meijering, E., Dzyubachyk, O. and Smal, I. (2012). Methods for Cell and Particle Tracking.Methods in Enzymology *504*, 183-200.

Murphy, K. P. (2012). Machine learning: a probabilistic perspective. Cambridge, MA. MIT press.

Namdaran P1, Reinhart KE, Owens KN, Raible DW, Rubel EW. (2012). Identification of modulators of hair cell regeneration in the zebrafish lateral line. J. Neurosci. *32*, 3516-3528.

Norden, C. (2017). Pseudostratified epithelia - cell biology, diversity and roles in organ formation at a glance. J. Cell Sci. 28.

Parinov, S., Kondrichin, I., Korzh, V. and Emelyanov, A. (2004). Tol2 transposon-mediated enhancer trap to identify developmentally regulated zebrafish genes *in vivo*. Dev. Dyn. *231*, 449-459

Pinto-Teixeira, F., Viader-Llargués, O., Torres-Mejía, E., Turan, M., González-Gualda, E., Pola-Morell, L., and López-Schier, H. (2015). Inexhaustible hair-cell regeneration in young and aged zebrafish. Biol. Open *4*, 903–909.

728 Romero-Carvajal A, Navajas Acedo J, Jiang L, Kozlovskaja-Gumbrienė A,
729 Alexander R, Li H, Piotrowski T. (2015). Regeneration of Sensory Hair Cells
730 Requires Localized Interactions between the Notch and Wnt Pathways. Dev.
731 Cell. *34*, 267-282.
732 Rosen, J.N., Sweeney, M.F., Mably, J.D. (2009). Microinjection of zebrafish
733 embryos to analyze gene function. J. Vis. Exp. *25*, 1115.
734 Rossi, A.M., Fernandes, V.M., Desplan, C.(2017). Timing temporal transitions
735 during brain development. Curr. Opin. Neurobiol. *42*, 84-92.
736 Sánchez, M., Ceci, M.L., Gutiérrez, D., Anguita-Salinas, C., Allende, M.L. (2016).
737 Mechanosensory organ regeneration in zebrafish depends on a population of
738 multipotent progenitor cells kept latent by Schwann cells. BMC Biol. *14*, 27.
739 Sasai, Y. (2013). Cytosystems dynamics in self-organization of tissue architecture.
740 Nature *493*, 318–326.
741 Sato, T., and Clevers, H. (2015). SnapShot: Growing Organoids from Stem Cells.
742 Cell *161*, 1700–1700.e1.
743 Seleit A, Krämer I, Riebesehl BF, Ambrosio EM, Stolper JS, Lischik CQ, Dross N,
744 Centanin L. (2017). Neural stem cells induce the formation of their physical niche
745 during organogenesis. Elife *6*, e29173.
746 Shin, J., Chen, J., and Solnica-Krezel, L. (2014). Efficient homologous
747 recombination-mediated genome engineering in zebrafish using TALE nucleases.
748 Development *141*, 3807–3818.

749 Simon, A., Berg, D., and Kirkham, M. (2009). Not lost in translation: Sensing the
750 loss and filling the gap during regeneration. Sem. Cell & Dev. Biol. *20*, 691–696.
751 Steiner, A.B., Kim, T., Cabot, V., and Hudspeth, A.J. (2014). Dynamic gene
752 expression by putative hair-cell progenitors during regeneration in the zebrafish
753 lateral line. Proc. Natl. Acad. Sci. U.S.A. *111*, E1393–E1401.
754 Turner DA, Baillie-Johnson P, Martínez-Arias A. (2016). Organoids and the
755 genetically encoded self-assembly of embryonic stem cells.Bioessays. *38*, 181-
756 191.
757 Wada H, Ghysen A, Asakawa K, Abe G, Ishitani T, Kawakami K. (2013). Wnt/Dkk
758 negative feedback regulates sensory organ size in zebrafish.Curr. Biol. *23*, 1559.
759 Wibowo, I., Pinto-Teixeira, F., Satou, C., Higashijima, S. -i., and López-Schier, H.
760 (2011). Compartmentalized Notch signaling sustains epithelial mirror symmetry.
761 Development *138*, 1143–1152.
762 Willyard, C. (2015). The boom in mini stomachs, brains, breasts, kidneys and more.
763 Nature *523*, 520–522.
764 Williams JA, Holder N. (2000). Cell turnover in neuromasts of zebrafish larvae.
765 Hear. Res. *143*(1-2), 171-181.
766 Wymeersch, F.J., Huang, Y., Blin, G., Cambray, N., Wilkie, R., Wong, F.C., and
767 Wilson, V. (2016). Position-dependent plasticity of distinct progenitor types in
768 the primitive streak. eLife *5*, e14830.
769 Xiao, Y., Faucherre, A., Pola-Morell, L., Heddleston, J.M., Liu, T.-L., Chew, T.-L.,
770 Sato, Sehara-Fujisawa, Kawakami, K., and López-Schier, H. (2015). High-

resolution live imaging reveals axon-glia interactions during peripheral nerve injury and repair in zebrafish. Dis. Model Mech. *8*, 553.

FIGURE LEGENDS

Figure 1. Geometric organization of the neuromast. (**A-C**) Schematic representation of a neuromast depicting (**A**) cell classes identifiable by expression of transgenic markers. Grey arrows indicate, respectively, (**B**) radial symmetry and (**C**) epithelial planar polarity. (**D-I**) Confocal images of cell-specific transgenic markers. (**D**) Alpl:mCherry marks mantle and interneuromast cells, (**E**) SqGw57A shows all supporting cells, (**F**) Cldnb:lynGFP marks all neuromast cells, (**G**) Sox2-GFP marks supporting and interneuromast cells, (**H**) SqET4 labels hair cells, and (**I**) Myo6b:actin-GFP highlights the planar polarization of the hair cells by decorating their apical stereocilia. Scale bars: 10 µm. (**J**) Images of dorsal (top) and lateral (bottom) views of a SqGw57A transgenic zebrafish larva, revealing the full complement of superficial neuromasts and their stereotypic position. (**K**) A single confocal section of the lateral view of a neuromast expressing GFP in supporting cells (Sox2-GFP) and a RFP in all nuclei (H2B-RFP). (**L**) Same neuromast in K showing RFP-marked nuclei. The white arrow indicates 4 cells (circled), which are target of the laser beam for ablation. (**M-P**) Four still images of the neuromast in L

over a period of five minutes, in which the laser-targeted cells are eliminated from the epithelium (white arrow).

Movie 1. A 20-minute videomicroscopic recording of a neuromast after laser-mediated ablation of supporting cells. Four laser-targeted cells (showing a dark spot in the nuclei from focal fluorescent-protein bleaching) are eliminated from the epithelium, which closes the wound. There is no noticeable collateral damage. Time resolution is one image per 30 seconds.

Figure 2. Zebrafish larvæ do not regenerate completely-ablated neuromasts. (**A-E**) Confocal images of a 7-day follow-up of the complete ablation of a neuromast in the double transgenic line *Tg[Cldnb:lynGFP; Alpl:mCherry]*. **(A)** The site of damage was identified over subsequent days by the position of an intact reference neuromast (white asterisk). (**B**) Laser-mediated cell ablation produced a wound 4 hours-post-injury (hpi). (**C-E**) This wound was replaced by a thread of mCherry(+) cells (white arrow) 1 day-post-injury (dpi), which did not change over the subsequent 6 days. (**F-J**) Confocal images over a 7-day time course after the ablation of a neuromast in the double transgenic line *Tg[Sox2:GFP; Alpl:mCherry]*. Identically to A-E, the complete ablation of the target neuromast results in a thin trail of interneuromast cells (white arrowheads) covering the damaged area (**K-N**). Scale bars: 10 μm.

Figure 3. Neuromasts have isotropic regenerative capacity. (**A**) Ablation of the posterior half of a neuromast. (**B-C**) The damage is resolved by cellular movement from the undamaged site 1dpi. (**D**) Neuromasts recover geometric order after 3 days and (**J**) return to homeostasis by 7dpi. Dashed lines in **A,F,K,P,U** delineate the ablated area. (**F-J**) Simultaneous ablation of the posterior half of a neuromast and the interneuromast cells flanking its anterior and posterior sides (n=5) led to a regeneration outcome identical to that of the experiment in **A-E**. Arrowheads in **F** point the location normally occupied by the interneuromast cells. (**K-O**) Neuromasts depleted from their dorsal half (n=6) also recover epithelial size, proportions and geometry in a manner indistinguishable from equatorial-side ablation after 7 days. (**P-T**) 7 days after their complete laser-mediated ablation, mantle cells regenerated for neuromasts to recover the mantle. (**U-Y**) The ablation of interneuromast cells flanking both sides of neuromasts that were depleted of mantle cells resulted in the same outcome (n=6). (**Z**) Quantification of the number of cells in regenerated neuromasts at 7 dpi. Number of neuromast cells was no statistically significant between groups of different damage regimes as determined by one-way ANOVA ($F(4,27)=1.013$, $p=0.4183$). Scatter plot shows mean±s.e.m.ns: non-significant. Scale bars: 10 μm.

Figure 3-figure supplement 1. Interneuromast cells do not regenerate. (**A-E**) The ablation of interneuromast cells adjacent to one flank of a neuromast resulted in the stretching of the last undamaged interneuromast cell (arrowhead) but does not

836 trigger interneuromast-cell proliferation or the reformation of interneuromast-cell
837 strings (n=14). (**F-J**) Likewise, the complete ablation of interneuromast cells in both
838 flanks from one neuromast to the next, generates a corresponding gap of
839 interneuromast cells that did not change over 7 days (n=8). Scale bars: 50 µm.
840
841 **Figure 4. Recovery of organ architecture after loss of tissue integrity.** (**A-E**)
842 Confocal images of a neuromast regenerating from 4-10 cells during a period of 7
843 days. Neuromasts recover radial symmetry 3 dpi (**D**), and original organ proportions
844 at 7 dpi (**E**). (**F-J**) Neuromasts reduced to 4-10 cells that were previously deprived
845 from adjacent interneuromast cells (INCs) (arrowheads in **F**), regenerated and
846 reformed radial symmetry (**H-I**) and proportions 7 dpi, despite maintaining a
847 reduced size (**J**). Dashed circles in **A,F** illustrate damaged areas. Scale bars: 10 µm.
848 (**K,N**) Total cell numbers in regenerating neuromasts over 7 days in the two
849 conditions depicted in **A-J**. (**L,O)** In the first 2 dpi neuromast consist almost
850 exclusively of supporting cells (green and red). Hair cells (blue) begin to appear
851 between at 2dpi. (**M,P**) Percentages of cell classes during a 7-day regeneration
852 period. Right after damage, neuromast experience an imbalance of cell proportions
853 that is re-established over the course of 3 days. Afterwards the neuromasts continues
854 to slowly increase total cell number at similar rates. The final proportion of cell
855 classes recapitulates that of the starting condition. Time points show mean±s.e.m.
856 [All except 4-10 cells] n=15, [All except 4-10 cells + INC] n=6. (**Q**) Top and (**R**)
857 lateral views of a triple-transgenic *Tg[Ncad: Ncad-EGFP; Alp:mCherry; H2A:H2A-*

858 *EGFP]* neuromast before injury. (**S**) Top and (**T**) lateral views of a regenerated
859 neuromast 7 days post injury (n=4). Basal location of nuclei and apical N-cadherin
860 enrichment evidence the apicobasal polarization of the organ. The accumulation of
861 N-cadherin (white arrowheads) in the regenerated neuromast shows that apical
862 constrictions are properly re-established during the process. (**U-V**) Maximal
863 intensity projection of a neuromast in the triple transgenic line *Tg[Cldnb:lynGFP;*
864 *SqGw57A; Alpl:mCherry]* prior to injury that eliminates all except 4 to 10 cells (**U**),
865 and the same neuromast 7 days after damage (**V**). (**W**) Hair-bundle staining with
866 rhodamine-phalloidin (colored in pink) reveals the coherent planar polarization of
867 the hair cells in the regenerated neuromast shown in **V**. (**X**) Confocal projection of a
868 neuromast before the removal of flanking interneuromast cells. (**Y**) Maximal
869 projection of a neuromast 48 hours after interneuromast-cell ablation and 24 hours
870 after neomycin treatment. (**Z**) Phalloidin staining of hair bundles of hair cells
871 regenerated in the absence of interneuromast cells, showing recovery of coherent
872 epithelial planar polarity. Scale bars: 10 µm.
873
874 **Figure 5. Long-term whole-organ single-cell tracking reveals cell-clone**
875 **formation during neuromast regeneration.** (**A**) Still images showing a
876 representative 100 hours time-lapse recording of a regenerating neuromast in
877 *Tg[Clndb:lynGFP; SqGw57A; Alpl:mCherry]* larva (left and middle panels).
878 Cellular clones that share a common founder cell are clustered and color-coded. Cell
879 trajectories reveal a concentric growth pattern (right panel). **(B)** Cell trackings at the

last recorded timepoints for 10 out of the total of 15 regenerated neuromasts. (**C**) Cell-lineage tracing from time-lapse movie shown in (**A**). Branching points symbolize cell divisions. The division of a founder cell generates two cells of the 1st generation. Subsequent divisions produce cells of the 2nd, 3rd and 4th generation. Cell classes are indicated with green (sustentacular), blue (hair) and red (mantle) colors. (**D**) Sustentacular founder cells undergo significantly more (p=3.59e-06, Mann-Whitney test) division rounds than mantle founder cells during 100 hours of neuromast regeneration. (**E**) The first division of sustentacular founder cells (n=76) occurs significantly earlier (p=1.13e-5, Mann-Whitney test) than that of mantle founder cells (n=16). (**F**) Sustentacular founder cells (n=76) generate all three neuromast cell classes whereas mantle founder cells (n=30) produce only mantle cells. (**G**) Out of 307 sustentacular cell divisions, 78% were self-renewing, 16% produced a pair of hair cells, 3% produced sustentacular cells that both became mantle cells within the next generation and 3% generated two sustentacular cells of which only one transited to mantle cell fate within the next generation. All 20 observed mantle cell divisions were self-renewing.

Movie 2. 100-hour time-lapse recording of a regenerating neuromast after severe ablation. A neuromast regenerates its original architecture from as few as 6 founder cells. Founder cells are identified by 1-6 (*n*) and their daughter cells receive *2n* and *2n+1* identities. Recording starts 4 hours post injury (hpi) and shows single focal planes. Time is in hours post injury.

Figure 6. Neuromast regeneration is not stereotypic and reveals different clone type compositions. (**A**) Proliferation is markedly isotropic during the first 60 hours of neuromast regeneration (n=348). (**B**) Homeostatic, dorso-ventral (DV) proliferative territories are restored after 60hpi (n=27). (**C**) 40% and 36% of the progeny from anterior (n=202) and posterior (n=173) founder cells crossed to the contralateral side (light grey) after 60 hours of regeneration. (**D**) Only 28% and 26% of the progeny from dorsal (n=199) and ventral (n=176) founder cells crossed to the contralateral side (light grey) during the same period of time. (**E**) Representative examples of different clone types extracted from time-lapse data. Sustentacular cells give rise to S, SM, SH, and SHM clones (color coded respectively with green, pink, cyan and orange) whereas mantle cells produce only pure mantle cell clones. (**F**) The clone composition of the 15 regenerated neuromasts is not stereotypic. The length of each bar represents the proportion of neuromast cells that belong to each clone. Neuromast 8 has been shown in Figure 5A,B. (**G**) The most frequent clones contain sustentacular and hair cells (SH, n=37 clones), followed by those with only sustentacular cells (S, n=21 clones). The third most frequent are composed by sustentacular and mantle cells (SM, n=12 clones). Clones containing all three cell classes were rare (SHM, n=2 clones).

Figure 7. Quantification of cell divisions during neuromast regeneration. (**A-B**) Equally spaced waves of coordinated sustentacular cell divisions (green) underlie

924 the recovery of neuromast cell size. Mantle cell divisions (red) occur occasionally
925 and do not follow the pattern of sustentacular cells. Proliferative waves correspond
926 to the coordinated divisions of cells from independent generations. (**C**) Cells from
927 the 1st and 2nd generation divide on average after cell cycles of 11±5 and 14±9
928 hours respectively (mean±s.d.). Coordination is lost at the 3rd generation when cell
929 cycles start to lengthen (26±18 hours, mean±s.d.). (**D**) Cell cycle length (11±3 hours,
930 mean±s.d.) is marginally influenced by regeneration time until 47 hours after injury,
931 when cycle length starts increasing proportionally with regeneration time. (**E**) Cell
932 cycle lengths (12±6 hours, mean±s.d.) do not correlate directly with neuromast size
933 until 24 neuromast cells. (**F**) S, SM and SH clones produce similar number of cells
934 ($p=0.68$, Kruskal Wallis test). In the box plots, the boundary of the box indicates the
935 25th and 75th percentile, respectively the black line within the box marks the
936 median. Whiskers above and below the box include points that are not outliers. (**G**)
937 Sustentacular founder cells of S, SM, and SH clones divide similarly early ($p=0.42$,
938 Kruskal Wallis test) after approximately 18 hours after neuromast injury. (**H**)
939 Sustentacular founder cells that produce SH (cyan) and S clones (green) are
940 distributed similarly around the center of the organ (at $x=y=0$). Those that generate
941 SM clones (pink) are localized further away from the center and are biased towards
942 the posterior side.
943
944 **Figure 8. Implementation of predictive machine-learning analysis.**

945 **(A)** Overview from experiments to prediction. Movies of neuromast regeneration
946 allow us to track every single cell over 100hpi and to generate a cell lineage from
947 these track points. Information covered in all tracks and lineages can be extracted as
948 features with which we train our random forest machine-learning classifier to predict
949 division or cell lineage fate. (**B**) Sustentacular founder cell choices between SH vs.
950 SM clones can be predicted with high accuracy (MCC=0.63±0.09, mean±s.d., n=15
951 bootstrapped samples) whilst choices between S and SH or SM clones are highly
952 inaccurate (MCC=0.19±0.11 and 0.15±0.10, mean±s.d., respectively, n=15
953 bootstrapped samples), based on 32 calculated features. (**C**) Features relative to the
954 position of the founder cells and their nearest cellular environment can discriminate
955 between SM and SH clone types. (**D**) Choices between SM/MM and HH divisions
956 can be predicted with high accuracy (MCC = 0.91±0.07, mean±s.d., n=15
957 bootstrapped samples) while those between SS and HH or SM/MM have low
958 accuracy (MCC=0.50±0.05 and 0.38±0.15, respectively, mean±s.d., n=15
959 bootstrapped samples) (**E**) Features describing the cell's position in relation to the
960 neuromast center and their proximity to other mantle cells have the highest influence
961 on the cell fate choices of a sustentacular cell. (**F**) SM/MM divisions (red) appear
962 predominantly at the periphery of the organ whereas HH divisions (blue) appear
963 proximal to the center. Sustentacular cell self-renewing divisions (SS, green) occur
964 mostly around the neuromast center, generating a ring-like pattern.
965

966 **Figure 8 – figure supplement 1. Comparison of different classification methods**

With 83.1% accuracy random forests perform best comparing features based ML algorithms on our data. We used the standard classification learners in MATLAB to obtain a first impression of the performance of possible ML approaches. We a 5-fold cross-validation we tested and compared the described methods.

Figure 8– figure supplement 2. Features used to predict SM vs SH clones sorted by predictive importance.

The bar plot shows all features used to predict SM vs. SH clones. They are sorted by their predictive importance and their error bars are generated by the used leave-one-out approach. The plots above exemplary show feature distributions of normalized distance to neuromast center (left) and average distance to mantle cells (right) for SM and SH clones.

Figure 8– figure supplement 3. All features used to predict SM/MM vs HH divisions sorted by predictive importance.

The bar plot shows all features used to predict SM/MM vs HH divisions. They are sorted by their predictive importance and their error bars are generated by the used leave-one-out approach. The plots above exemplary show feature distributions of minimal distance to mantle cells (left) and normalized distance to neuromast center (right) for SM/MM and HH divisions.

Figure 9. Schematic model of neuromast regeneration. The top diagram exemplifies the architecture of an intact neuromast. A, B and C indicate three types of injury: A when mantle cells are lost, B when hair cells are ablated, and C when a localized combination of all three cell classes is lost. Under the model that we present, radial symmetry serves to localize damage and canalize regeneration spatially. If central hair cells are lost (A), radial symmetry is maintained for sustentacular progenitors to regenerate hair cells centripetally (grey arrows in A). If outer cells are lost (B), radial symmetry is also maintained for the generation of progeny that will acquire mantle fate and propagate centrifugally to reform the outer rim of the neuromast (grey arrows in B). Upon asymmetric damage, however, the radial symmetry is partially broken (C). The neuroepithelium repolarizes along an injured-intact axis, which canalizes regeneration towards the damaged areas (grey arrows in C). Individual cells are color-coded (mantle cells in red, sustentacular cells in light blue, and hair cells in green), and in each case we indicate the type of division that the intact cells undergo: symmetric (S) when they produce two equivalent cells or self-renew, and asymmetric (A) when their division generates sibling cells that differentiate into different classes.

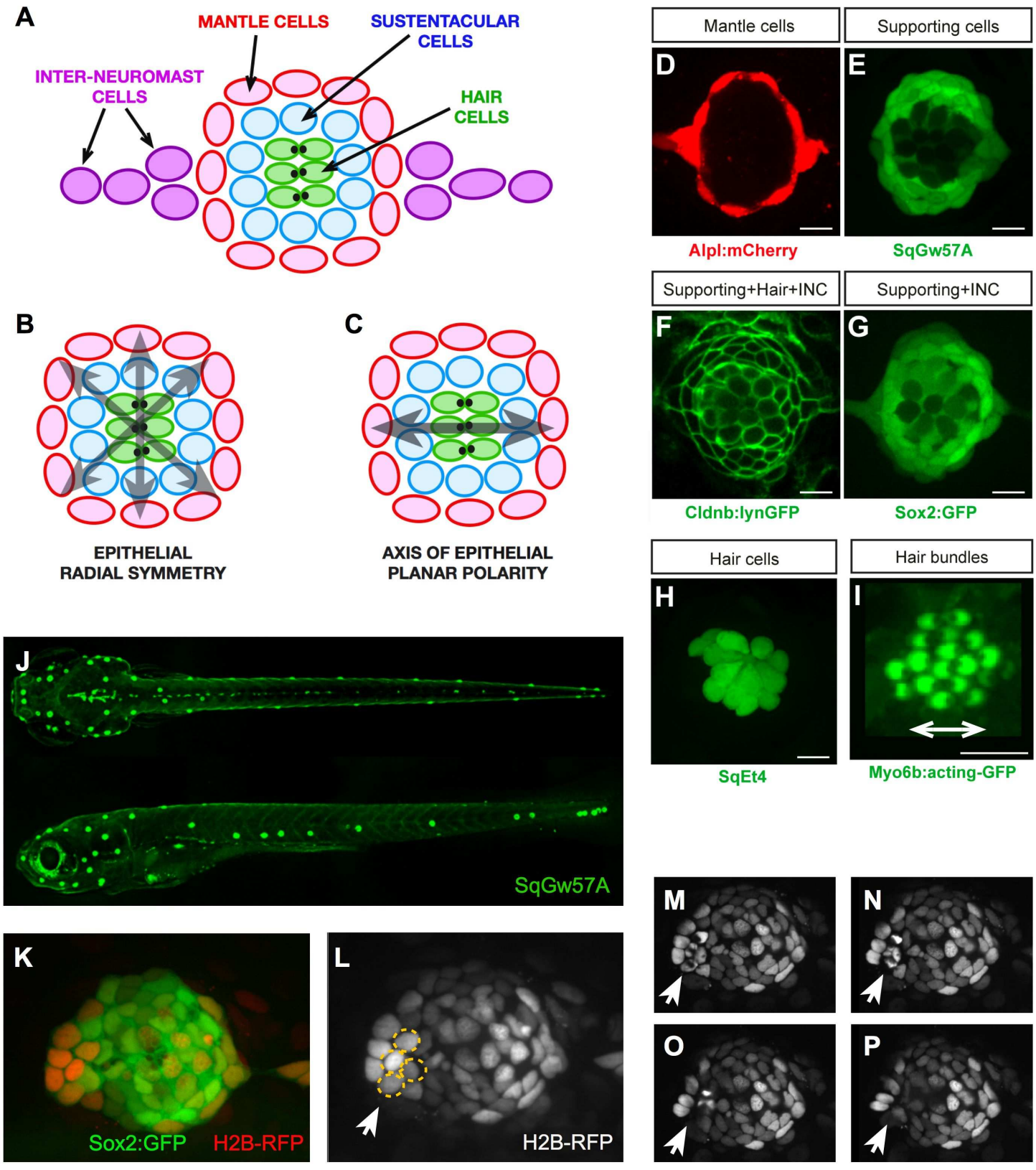
A
MANTLE CELLS
SUSTENTACULAR CELLS
INTER-NEUROMAST CELLS
HAIR CELLS
B
EPITHELIAL RADIAL SYMMETRY
C
AXIS OF EPITHELIAL PLANAR POLARITY
Mantle cells
Supporting cells
D
E
Alpl:mCherry
SqGw57A
Supporting+Hair+INC
Supporting+INC
F
G
Cldnb:lynGFP
Sox2:GFP
Hair cells
Hair bundles
H
I
SqEt4
Myo6b:acting-GFP
J
SqGw57A
K
Sox2:GFP H2B-RFP
L
H2B-RFP
M
N
O
P

figure 1

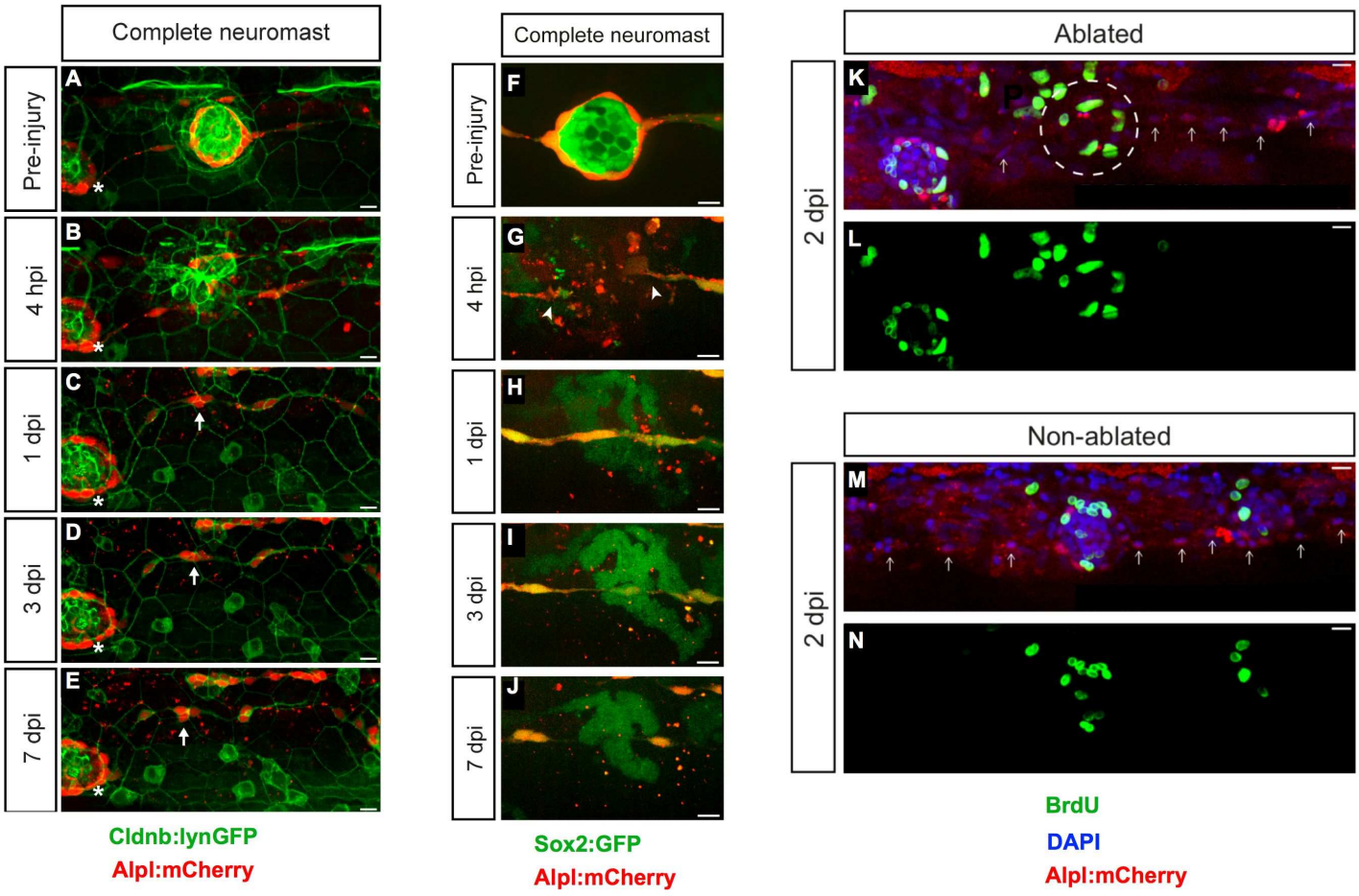
Complete neuromast
Pre-injury
4 hpi
1 dpi
3 dpi
7 dpi
A
B
C
D
E
Cldnb:lynGFP
Alpl:mCherry
Complete neuromast
F
G
H
I
J
Sox2:GFP
Alpl:mCherry
Ablated
Non-ablated
2 dpi
K
L
M
N
BrdU
DAPI
Alpl:mCherry

figure 2

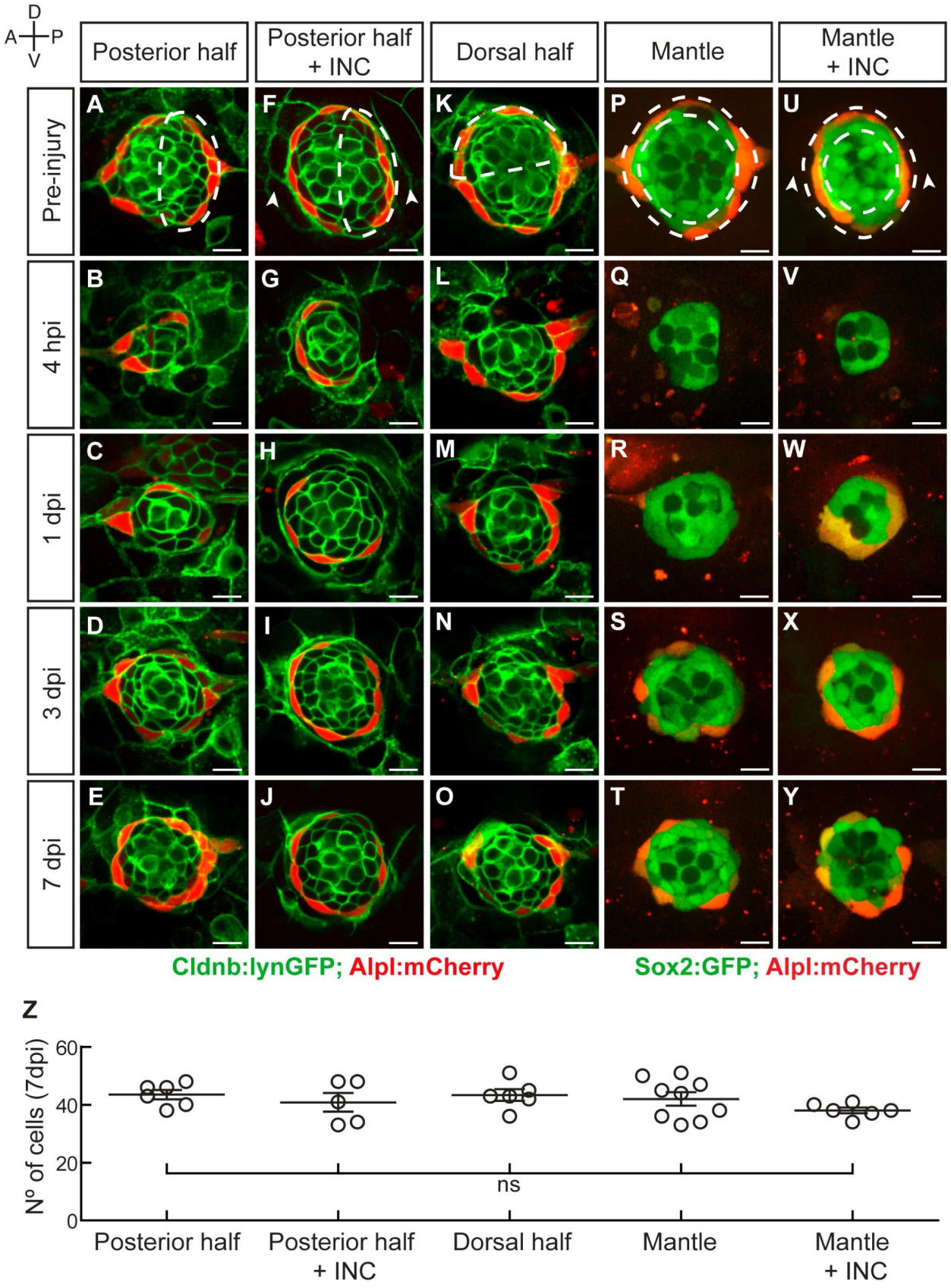
D
A
P
V
Posterior half
Posterior half + INC
Dorsal half
Mantle
Mantle + INC
Pre-injury
4 hpi
1 dpi
3 dpi
7 dpi
A
F
K
P
U
B
G
L
Q
V
C
H
M
R
W
D
I
N
S
X
E
J
O
T
Y
Cldnb:lynGFP; Alpl:mCherry
Sox2:GFP; Alpl:mCherry
Z
Nº of cells (7dpi)
60
40
20
0
ns
Posterior half
Posterior half + INC
Dorsal half
Mantle
Mantle + INC

figure 3

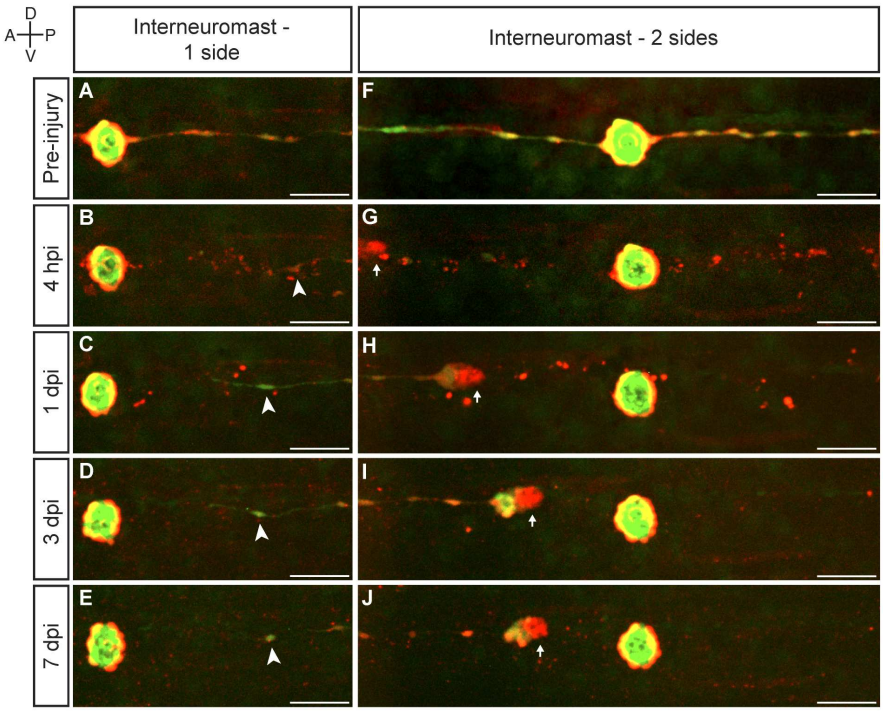

Sox2:GFP; Alpl:mCherry

figure 3 supp. 1

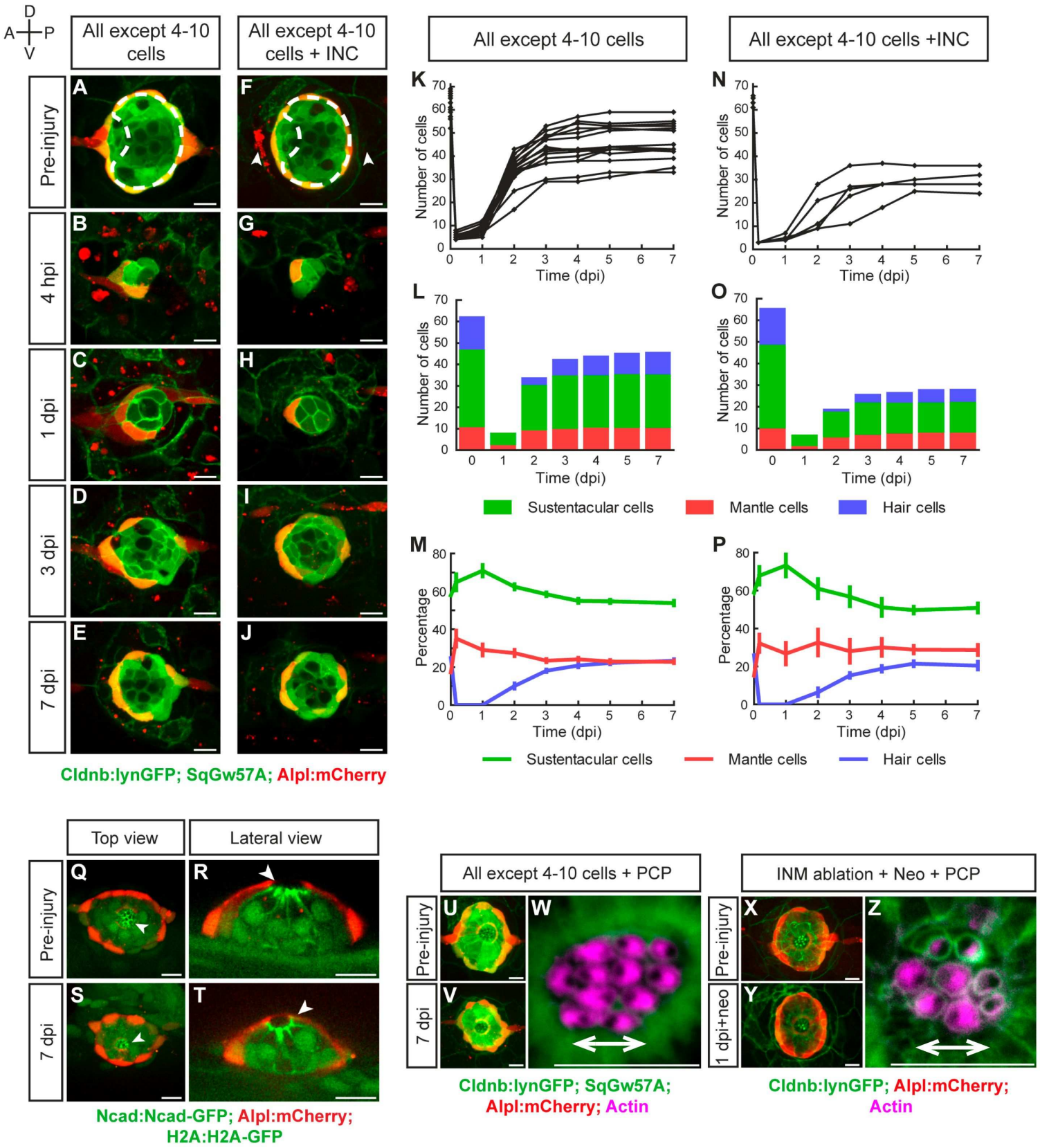
D
A
P
V
All except 4-10 cells
All except 4-10 cells + INC
Pre-injury
4 hpi
1 dpi
3 dpi
7 dpi
A
B
C
D
E
F
G
H
I
J
Cldnb:lynGFP; SqGw57A; Alpl:mCherry
All except 4-10 cells
All except 4-10 cells +INC
K
N
Number of cells
Time (dpi)
L
O
M
P
Percentage
Sustentacular cells
Mantle cells
Hair cells
Top view
Lateral view
Q
R
S
T
Ncad:Ncad-GFP; Alpl:mCherry; H2A:H2A-GFP
All except 4-10 cells + PCP
INM ablation + Neo + PCP
U
V
W
X
Y
Z
1 dpi+neo
Cldnb:lynGFP; SqGw57A; Alpl:mCherry; Actin
Cldnb:lynGFP; Alpl:mCherry; Actin

figure 4

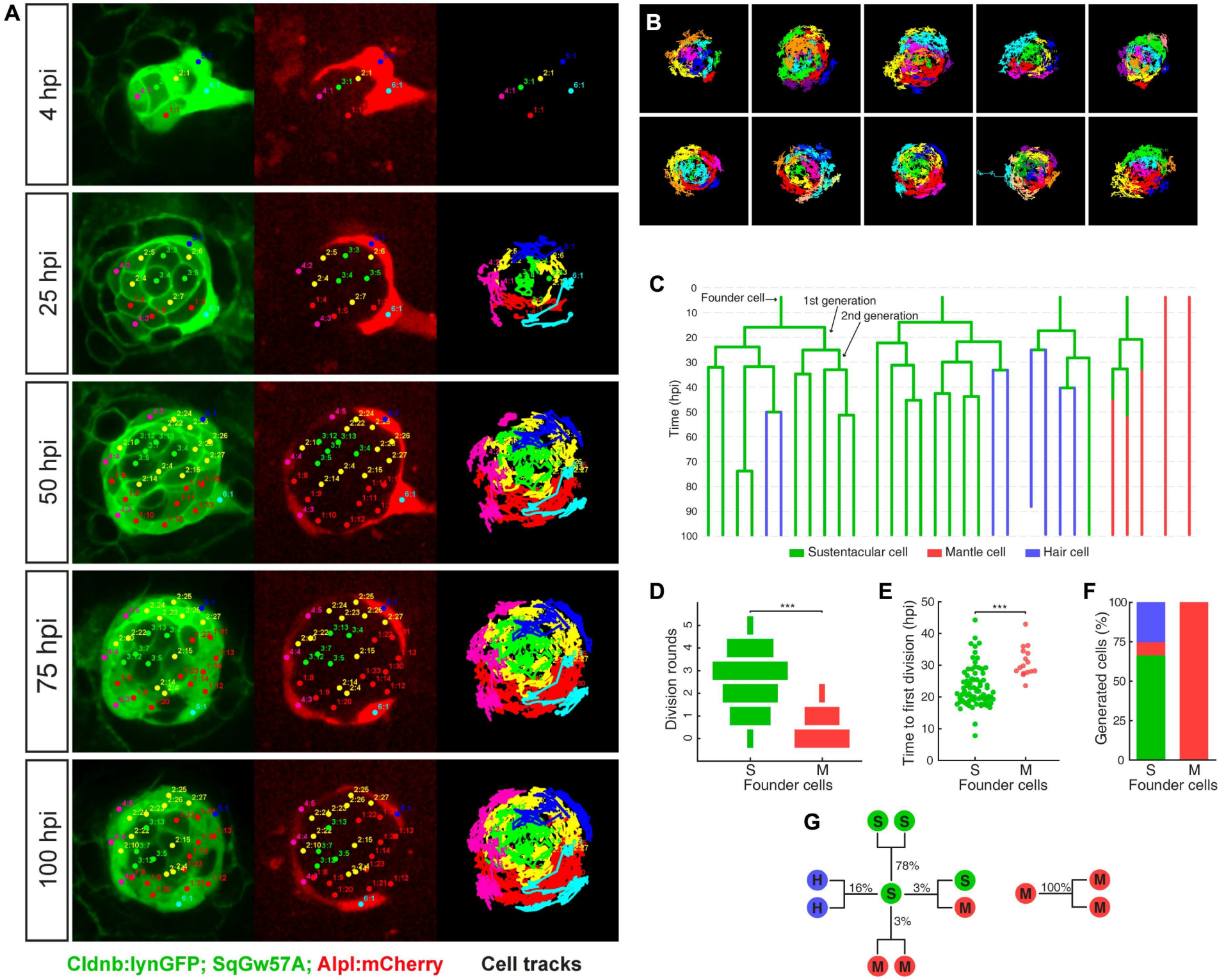
A
4 hpi
25 hpi
50 hpi
75 hpi
100 hpi
Cldnb:lynGFP; SqGw57A; Alpl:mCherry
Cell tracks
B
C
Founder cell
1st generation
2nd generation
Time (hpi)
Sustentacular cell
Mantle cell
Hair cell
D
Division rounds
S
M
Founder cells
***
E
Time to first division (hpi)
S
M
Founder cells
***
F
Generated cells (%)
S
M
Founder cells
G
78%
16%
3%
3%
100%

figure 5

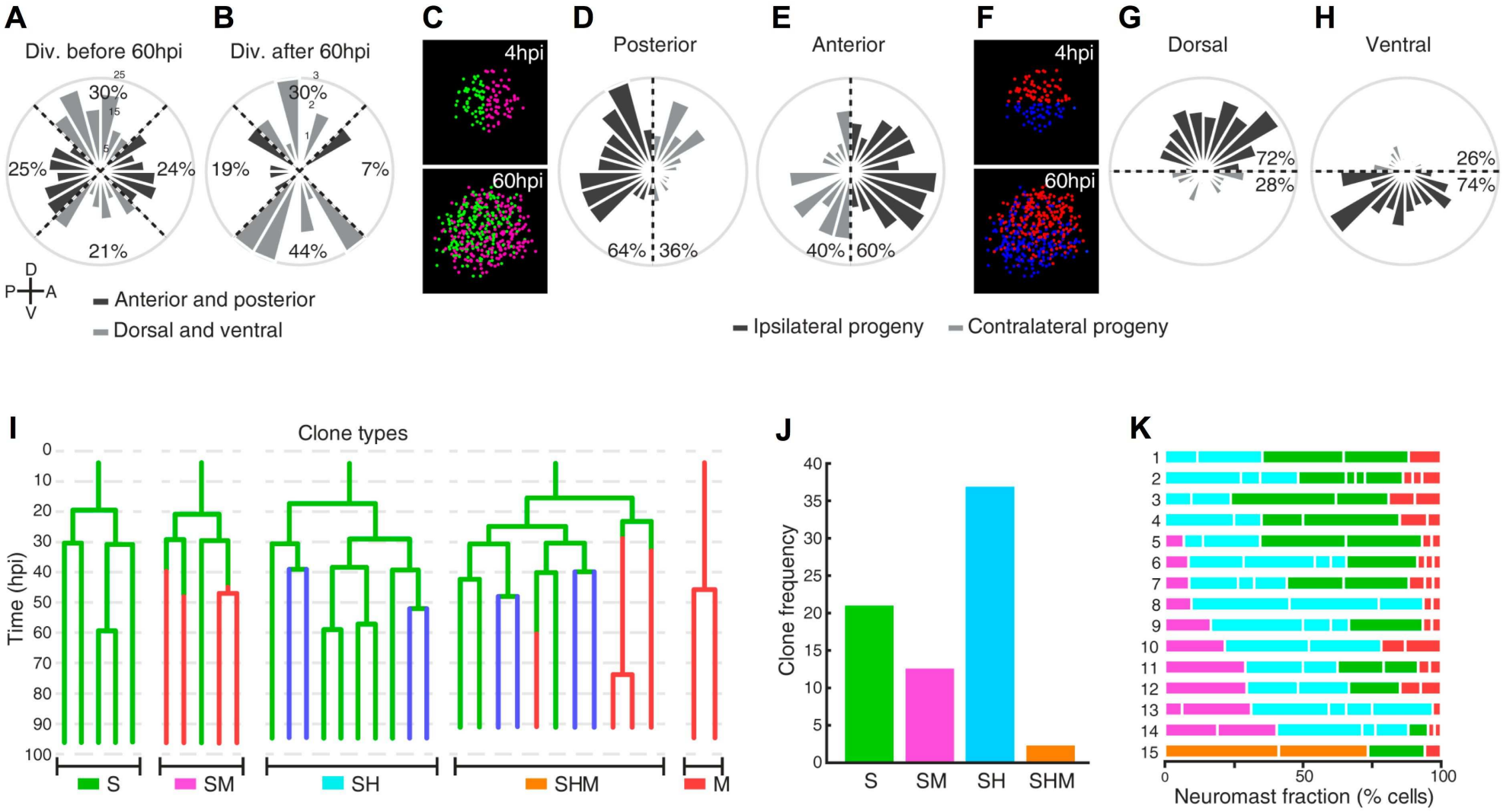
A
Div. before 60hpi
30%
25%
24%
21%
B
Div. after 60hpi
30%
19%
7%
44%
D
P
A
V
Anterior and posterior
Dorsal and ventral
C
4hpi
60hpi
D
Posterior
64%
36%
E
Anterior
40%
60%
F
4hpi
60hpi
G
Dorsal
72%
28%
H
Ventral
26%
74%
Ipsilateral progeny
Contralateral progeny
I
Clone types
Time (hpi)
S
SM
SH
SHM
M
J
Clone frequency
S
SM
SH
SHM
K
Neuromast fraction (% cells)

figure 6

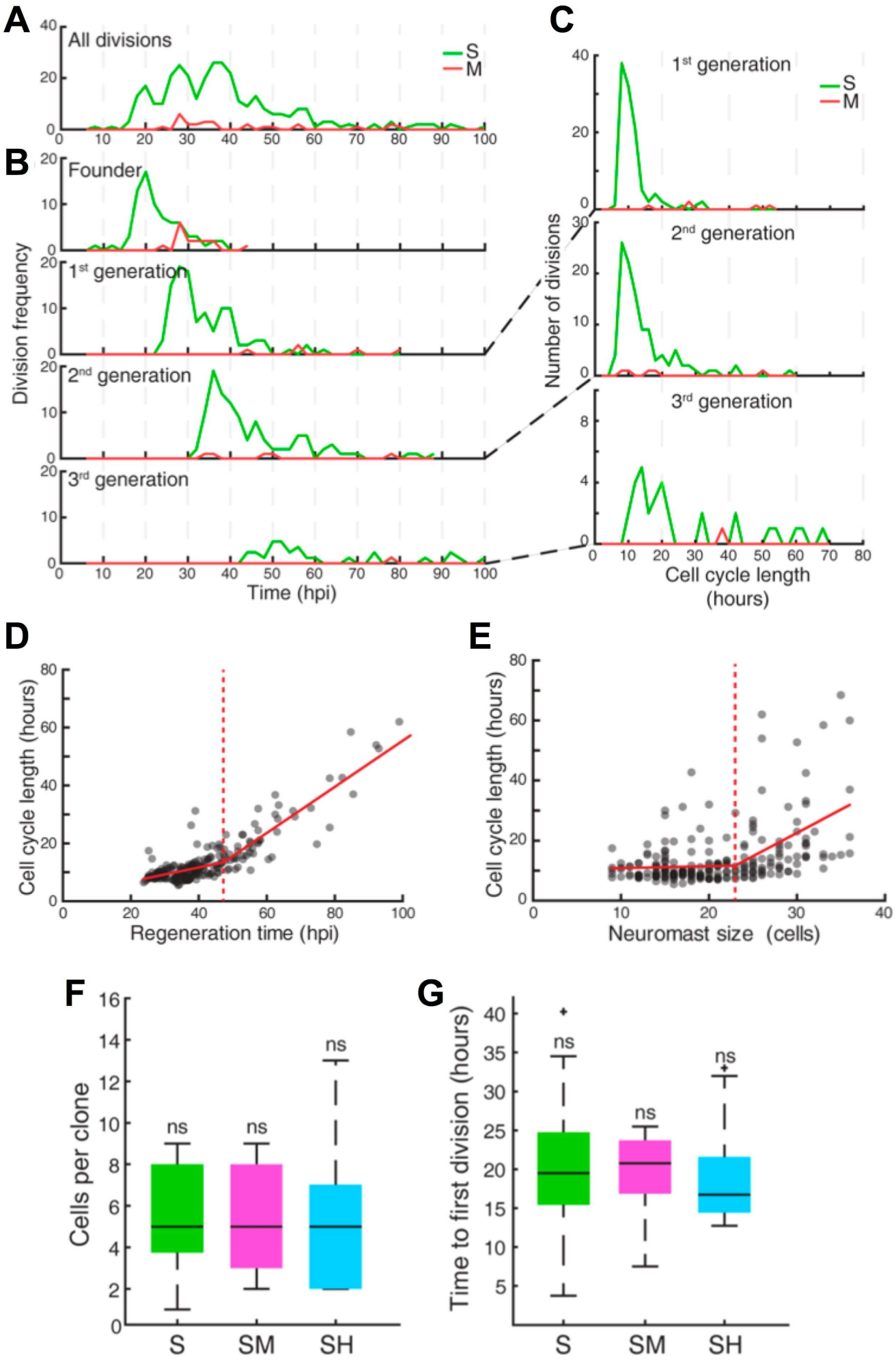
A
All divisions
S
M
B
Founder
1st generation
2nd generation
3rd generation
Division frequency
Time (hpi)
C
1st generation
2nd generation
3rd generation
Number of divisions
Cell cycle length (hours)
D
Cell cycle length (hours)
Regeneration time (hpi)
E
Cell cycle length (hours)
Neuromast size (cells)
F
Cells per clone
ns
S
SM
SH
G
Time to first division (hours)
ns
S
SM
SH

figure 7

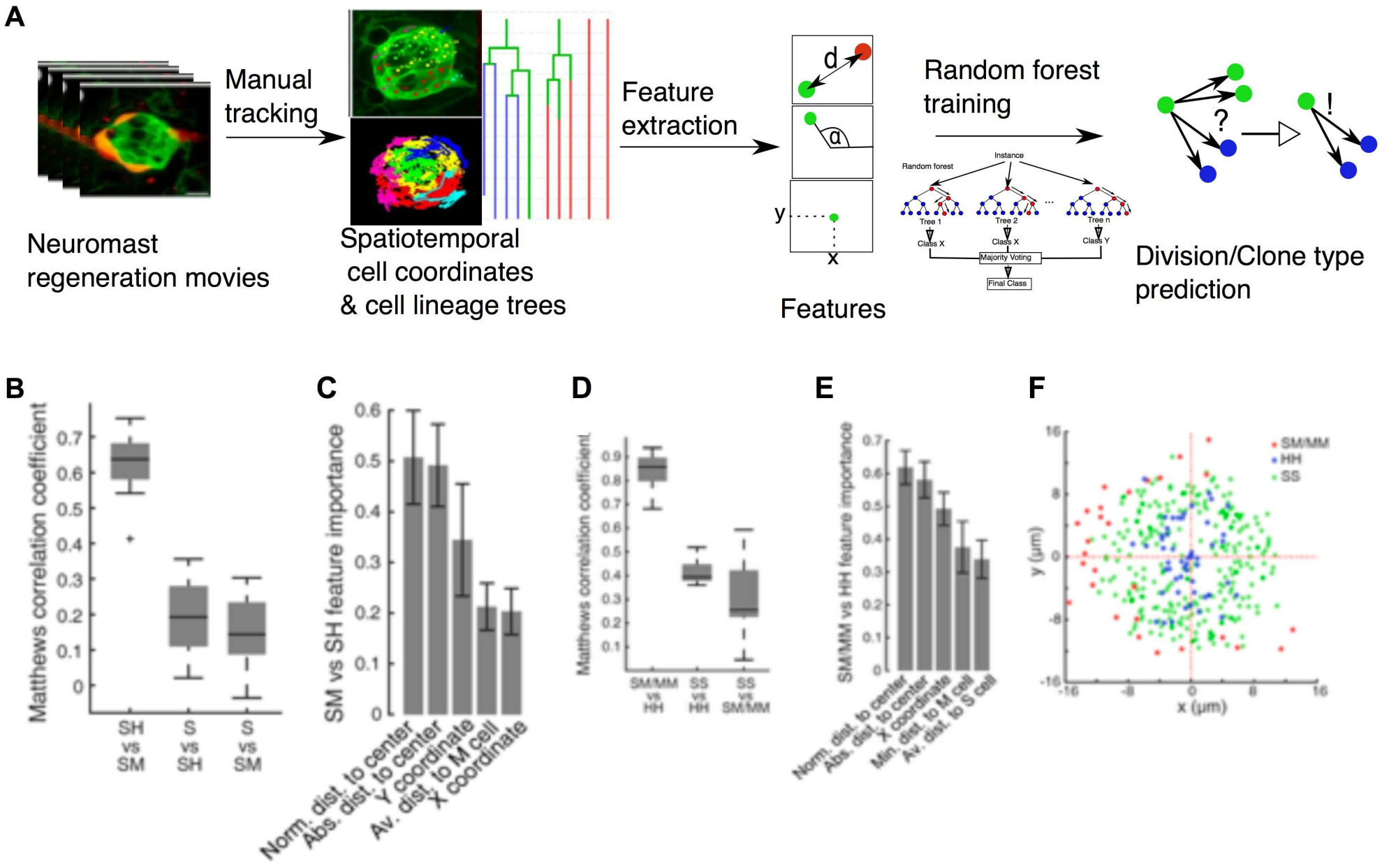
A
Manual tracking
Neuromast regeneration movies
Spatiotemporal cell coordinates & cell lineage trees
Feature extraction
d
α
y
x
Features
Random forest training
Random forest
Instance
Tree 1
Tree 2
Tree n
Class X
Class X
Class Y
Majority Voting
Final Class
Division/Clone type prediction
B
Matthews correlation coefficient
SH vs SM
S vs SH
S vs SM
C
SM vs SH feature importance
Norm. dist. to center
Abs. dist. to center
Y coordinate
Av. dist. to M cell
X coordinate
D
Matthews correlation coefficient
SM/MM vs HH
SS vs HH
SS vs SM/MM
E
SM/MM vs HH feature importance
Norm. dist. to center
Abs. dist. to center
X coordinate
Min. dist. to M cell
Av. dist. to S cell
F
SM/MM
HH
SS
y (µm)
x (µm)

figure 8

Method	Accuracy
Random Forest	**83.1%**
Boosted Trees	82.4%
Medium Tree	81.1%
Complex Tree	80.8%
Subspace Discriminant	80.8%
Simple Tree	80.1%
Linear SVM	78.5%
Quadratic SVM	78.5%
Cubic SVM	78.5%
Fine Gaussian SVM	78.5%
Medium Gaussian SVM	78.5%
Coarse Gaussian SVM	78.5%
Fine KNN	78.5%
Medium KNN	78.5%
Coarse KNN	78.5%
Cosine KNN	78.5%
Cubic KNN	78.5%
Weighted KNN	78.5%
Subspace KNN	76.6%

figure 8 supp. 1

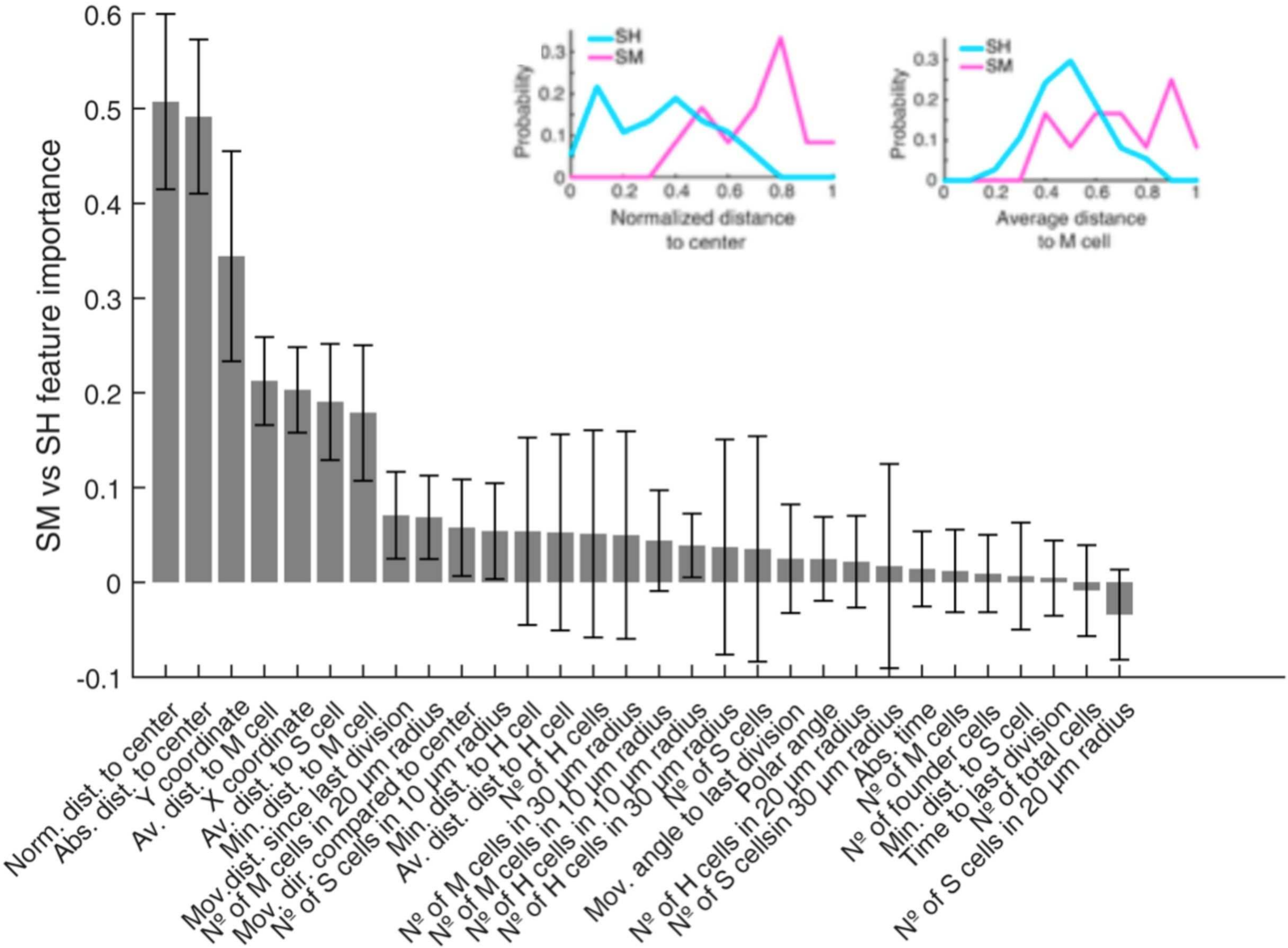

figure 8 supp. 2

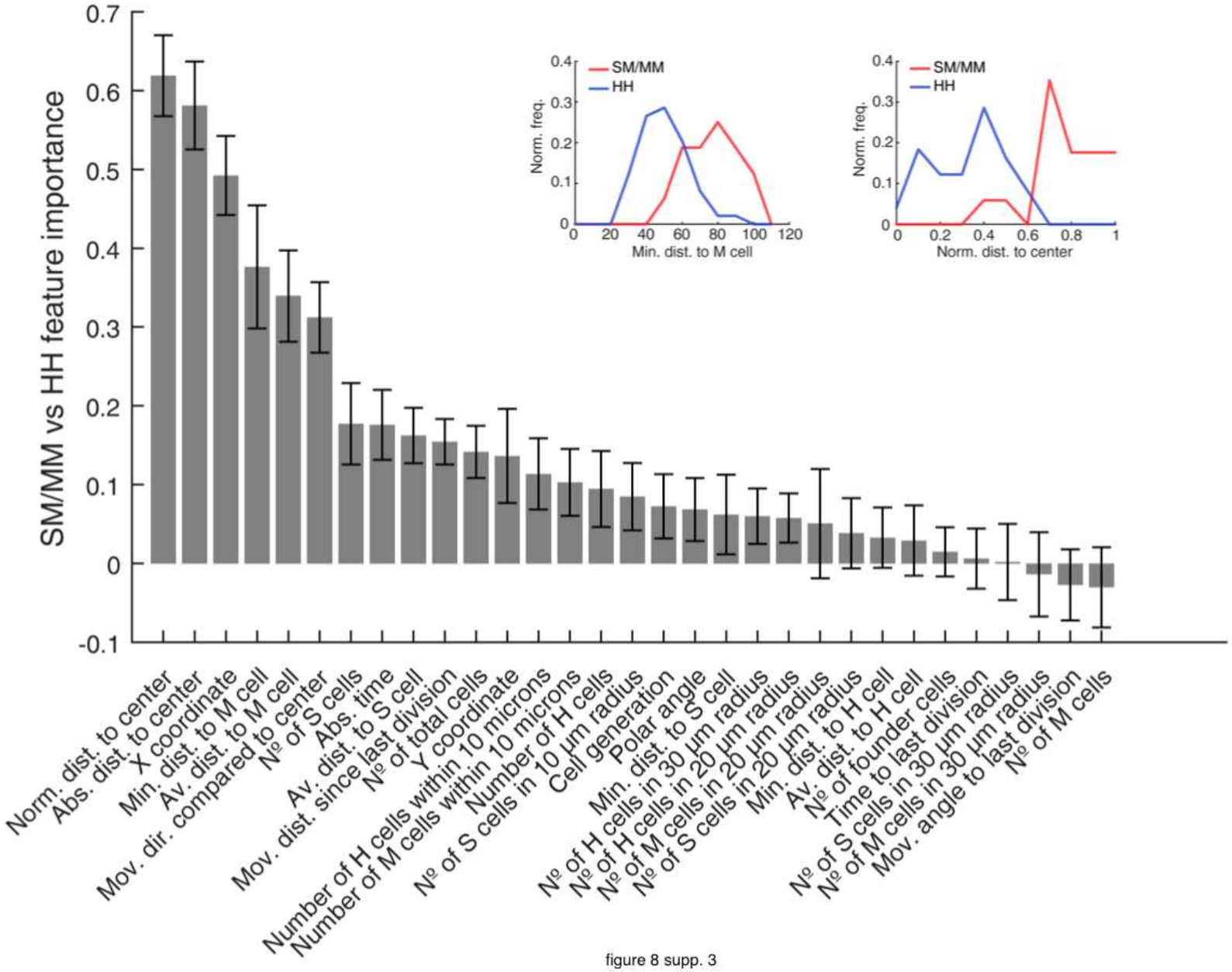

figure 8 supp. 3

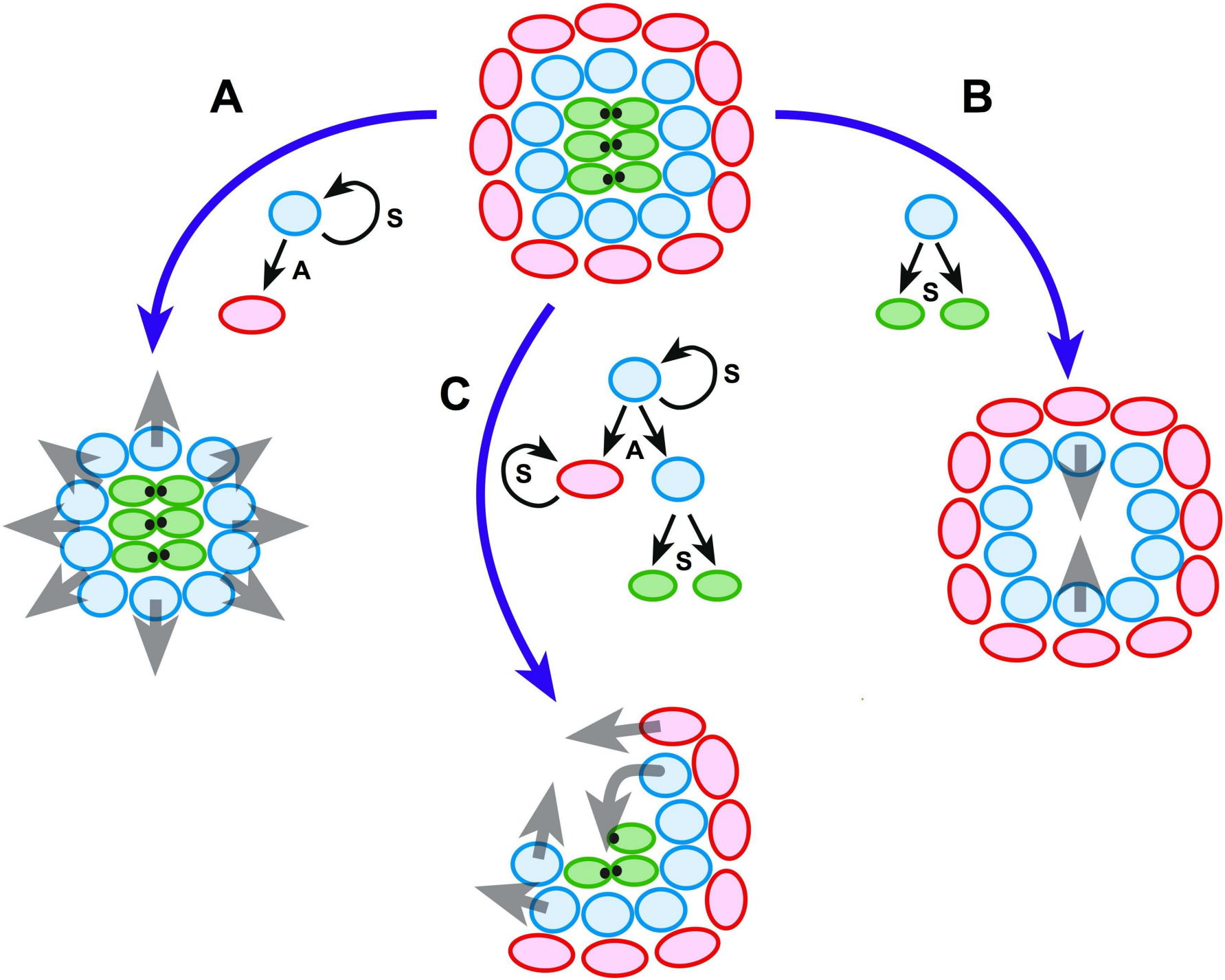

figure 9